DISEASES AND DISORDERS

# Hepatic hypertension on-a-chip identifies GPR116 as a hydrostatic pressure mechanosensor to regulate vascular injury in cirrhosis

**Yi Long[1,2]†, Kaini Liang[1]†, Yudi Niu[1]†, Rui Wang[3], Ruiquan Liu[4], Yan Zhang[1], Yanxiao Ao[1,5], Yuhong Jin[1], Zhaozhao Wu[1], Bingjie Wu[1], Zhiqiang Liu[1], Xin Zhang[6], Xiangyu Liu[6], Xiaolong Qi[7,8], Bin Liu[9], Yanan Du[1,2,5,10]***

**Cirrhosis-associated portal hypertension drives vascular injury, yet the pathogenesis mediated by abnormal hydrostatic pressure (HP) remains unclear due to the absence of in vitro models replicating the cirrhotic perivascular mechanical microenvironment. Here, we developed 2D static and 3D dynamic "hepatic hypertension on-a-chip" (HH chip) systems replicating cirrhotic hemodynamics and matrix properties. The HH chip realized integration and decoupled regulation of HP, shear stress, and matrix stiffness. Liver sinusoidal endothelial cells (LSECs) exhibited HP-induced damage exclusively on stiff matrices, recapitulating cirrhotic degeneration phenotypes and genotypes. Using the HH chip, we identified GPR116 as the key HP mechanosensor in LSECs and delineated its downstream mechanotransduction pathway driving cellular injury. Genetic silencing of GPR116 protected endothelial cells from HP-induced damage both in vitro and in cirrhotic murine models. Cell- and gene-based therapies targeting GPR116 significantly attenuated cirrhosis progression. The HH chip can accelerate pathological investigation, target identification, and therapeutic development for hypertension-associated diseases.**

## INTRODUCTION

Cirrhosis is an irreversible consequence of chronic liver disease, involving extensive fibrosis and restructuring of liver architecture, leading to portal hypertension (*1*). Portal hypertension exacerbates liver damage by promoting splanchnic vasodilation and increased blood inflow. The liver vasculature, burdened by elevated hydrostatic pressure (HP), leads to dysfunction in liver sinusoidal endothelial cells (LSECs), fostering severe clinical manifestations like ascites, variceal bleeding, and hepatic encephalopathy (*2*). Annually, this results in an estimated 1.2 million deaths worldwide (*1*). Despite this, the pathophysiological mechanisms of cirrhosis and portal hypertension remain poorly understood, and treatment options are limited, with no Food and Drug Administration–approved drugs beyond liver transplantation (*3*). Thus, exploring promising therapeutic targets and strategies is crucial.

Emerging research highlights the potential of antiangiogenic therapy in the early stages of liver fibrosis (*4*, *5*). Angiogenesis, triggered by liver injury and mechanical disturbances (*6*–*8*), appears to be a promising target. However, despite angiogenesis being evident in early fibrosis via corrosion casting and micro–computed tomography (μCT) imaging, it contrasts with the vascular sparsity observed in cirrhosis (*9*). This difference suggests that the diminished effectiveness of antiangiogenic therapy as cirrhosis progresses may be linked to vascular degeneration (*6*).

Substantial changes to the liver's mechanical microenvironment in cirrhosis, primarily through the excessive deposition of extracellular matrix (ECM), increase matrix stiffness and, combined with elevated portal pressure, alter the morphology and function of LSECs (*10*). Existing in vitro microphysiological systems (MPSs) have replicated angiogenesis in early fibrosis by regulating matrix stiffness (*6*, *11*) and modeled impaired LSECs homeostasis by modulating hydrodynamic pressure (*12*). However, solely adjusting this one mechanical factor fails to reproduce the vascular degeneration observed in cirrhosis (*6*), underscoring the need for improved models that couple multiple mechanical stimuli to better mimic the in vivo microenvironment.

To address these challenges, we developed the hepatic hypertension on-a-chip (HH chip), a MPS that simulates the distinctive hemodynamics and matrix characteristics of cirrhosis. This system, encompassing both two-dimensional (2D) static and 3D dynamic configurations, allows for the comprehensive simulation of the hepatic microenvironment under cirrhotic conditions. By facilitating independent adjustments of HP, shear stress, and matrix stiffness, the HH chip marks a notable advance over existing in vitro liver vascular mechanobiological models.

Additionally, mechanosensors, which convert mechanical signals into biochemical signals that influence cellular functions, play a crucial role in both physiological and pathological processes. Membrane proteins such as PIEZO1, PIEZO2, and TRPV4 (*13*), along with G protein–coupled receptors (GPCRs) like GPR68 (*14*), the histamine H1 receptor (*15*), angiotensin II type 1 receptor (*16*), and the apelin receptor (*17*), function as mechanosensors regulating various cellular

---

[1]School of Biomedical Engineering, Tsinghua-Peking Joint Center for Life Sciences, Tsinghua University, Beijing 100084, China. [2]Joint Graduate Program of Peking-Tsinghua-National Institute of Biological Science, Tsinghua University, Beijing 100084, China. [3]4+4 Medical Doctor Program, Chinese Academy of Medical Sciences and Peking Union Medical College, Beijing 100730, China. [4]Department of Plastic Surgery, Sun Yat-sen Memorial Hospital, Sun Yat-sen University, Guangzhou, China. [5]State Key Laboratory of Membrane Biology-Membrane Structure and Artificial Intelligence Biology Branch, China. [6]School of Pharmaceutical Sciences, Tsinghua University, Beijing 100084, China. [7]Center of Portal Hypertension, Department of Radiology, Zhongda Hospital, Medical School, Southeast University, Nurturing Center of Jiangsu Province for State Laboratory of AI Imaging and Interventional Radiology (Southeast University), Nanjing, China. [8]Basic Medicine Research and Innovation Center of Ministry of Education, Zhongda Hospital, Southeast University; State Key Laboratory of Digital Medical Engineering, Nanjing, China. [9]Department of Hepatobiliary Surgery, The First Affiliated Hospital of Kunming Medical University, Kunming 650032, China. [10]National Key Laboratory of Kidney Diseases, Beijing 100853, China.
*Corresponding author. Email: duyanan@tsinghua.edu.cn

†These authors contributed equally to this work.

responses. Located in low-pressure areas, LSECs are highly sensitive to minor fluctuations in sinusoidal pressure (*12*, *18*, *19*). Yet, it remains unclear which specific mechanosensors respond to elevated HP in LSECs during cirrhosis.

The HH chip distinctly addresses the need for in vitro models that accurately replicate the mechanical stresses imposed by increased portal pressure on liver vasculature. By using the HH chip, we observed significant manifestations of LSEC damage under abnormal HP conditions, particularly on a stiff matrix, mirroring the degenerative changes in LSECs associated with cirrhosis. Moreover, our research identified GPR116 as a critical mechanosensor in LSECs, integral to regulating the mechanotransduction pathways that mediate cellular responses to mechanical stress. This systematic exploration facilitated by the HH chip not only deepens our understanding of the mechanisms underlying vascular injuries in cirrhosis but also accelerates the discovery of therapeutic targets and drug screening for hypertension-related diseases. This study underscores the transformative potential of MPS in disease modeling and pharmaceutical development.

## RESULTS

### Establishment of the mechanotransduction-modulated HH chip

To investigate the responsiveness of hepatic blood vessels to pressure variations during fibrosis, we developed both 2D static and 3D dynamic HH chip models. These models are designed to emulate the mechanical interplay among LSECs, HP, shear stress, and matrix stiffness, reflecting the conditions of a fibrotic liver (Fig. 1, A to H).

The 2D static HH chip incorporates an array of well-ventilated pressure chambers crafted from polydimethylsiloxane (PDMS) (Fig. 1B and fig. S1D). As cirrhosis progresses, matrix stiffness rises from 200 Pa to 11 kPa (*20*–*22*), alongside a rise in the hepatic venous pressure gradient from 5 to 20 mmHg (*12*, *23*). Clinically, these changes serve as the gold standard for diagnosing portal hypertension in cirrhosis. Within these chambers, LSECs cultured on polyethylene glycol diacrylate (PEGDA) hydrogel substrates of variable stiffness (200 to 11,000 Pa) demonstrated distinctive morphologies upon exposure to a pressure gradient (0 to 60 mmHg) for 4 hours, after an initial 12-hour culture period. (Fig. 1C and fig. S1, A to C). Cells on softer (200 Pa) substrate retained a rounded morphology and exhibited inhibited migration. Conversely, cells on 1.5-kPa substrates, when subjected to increased pressure, formed angiogenic tip cells and tight junctions. At 10 mmHg, these activated cells organized stress fibers and focal adhesions, indicating enhanced migratory capacity and capillarization (*6*). At higher stiffness (11 kPa), the cells showed intercellular junctions and stress fibers with sparse focal adhesions. At 20 mmHg, cell numbers markedly decreased. The remaining cells contracted and aggregated into clusters, coinciding with the disappearance of focal adhesions, assuming an apoptosis-like morphology and loss of migratory ability (Figs. 1C and 2A and table S1).

The 3D dynamic HH chip accurately replicated the spatial structure and mechanical microenvironments of hepatic venules in vivo (Fig. 1, D to H). To emulate elevated loss tangent of matrix viscoelasticity from 0.03 to 1 during the cirrhotic (*24*–*26*), we adjusted the concentration and cross-linking degree of type I collagen (fig. S1, E and F). Additionally, fluidic resistors were integrated to the model, enabling precise control of the intratubular pressure from 5 to 20 mmHg while maintaining a shear stress of 12 dyne/cm$^2$ (*27*) to simulate portal hypertension (Fig. 1E and fig. S1H). Under perfusion culture, LSECs cultured within both soft (non–cross-linked, loss tangent of 0.091) and stiff (cross-linked, loss tangent of 0.551) 3D collagen lumens formed stable 3D tubular structures and intact vascular barrier (Fig. 1, F to H). At a low pressure of 5 mmHg, there was negligible change in cell numbers across both vessel types. However, at 20 mmHg, the soft vessels exhibited dilation, potentially compensating for the increased pressure and enhancing cell adhesion. In contrast, the cells in the stiff vessels showed partially detachment (Fig. 1H), a response consistent with observations from the 2D HH chip under similar high-pressure and high-stiffness conditions (Fig. 1C and fig. S1G).

### The HH chips reveal matrix stiffness–dependent HP stimulation can induce LSEC injury

To elucidate the underlying mechanisms of LSECs reduction in high-stiffness and high-pressure conditions that mimic the cirrhotic microenvironment, we used both 2D and 3D HH chips.

In 2D static HH chips, flow cytometry and gene expression analyses revealed that cells on soft substrates (1.5 kPa) experienced minimal damage under high-pressure (20 mmHg) stimulation. In contrast, high-pressure stimulation on stiffer substrates (11 kPa) significantly damaged LSECs (Fig. 2B). Cells on soft substrates exhibited a low initial Young's modulus (396.2 Pa), which increased to 458.0 Pa under high pressure. Conversely, cells on stiff substrates displayed a higher initial Young's modulus (687.6 Pa) but underwent apoptosis when subjected to high pressure, leading to a decreased Young's modulus of 551.3 Pa (Fig. 2C). Through scanning electron microscopy analysis of primary LSEC (pLSEC) fenestrations, soft substrate-cultured cells maintained abundant 3D fenestrations (mean area of ~0.005 μm$^2$). Under HP, structural disruption increased fenestrae area (~0.15 μm$^2$) and large fenestrae frequency, although porosity remained unchanged. In contrast, stiff substrate–cultured LSECs adopted flattened morphologies with similar baseline fenestrae areas (~0.005 μm$^2$). Pressure application induced architectural disorganization, generating abundant sub-0.005-μm$^2$ pores and significantly reduced porosity (Fig. 2, E to G). These findings suggested that cells on softer substrates more effectively withstand HP-induced damage, whereas cells on stiffer substrates sustain damage due to their inability to adapt to the elevated pressure.

In the 3D dynamic HH chip, cells in both soft and stiff vessels exposed to 5-mmHg pressure showed minimal apoptotic activity. However, at 20 mmHg, cells in the stiff vessels partially detached, remaining cells underwent apoptosis, increasing 3D lumen permeability and disrupting vascular barrier integrity (Fig. 2, K and L). Additionally, we found that genes related to cellular damage were highly expressed under conditions of high stiffness and high HP in both 2D and 3D HH chips (Fig. 2, D and M). These findings revealed that the HH chip recapitulates LSEC injury induced by stiffness-dependent HP in a simulated cirrhotic environment.

### The HH chips recapitulate cirrhotic vascular genotypic features

To validate whether HH chips can recapitulate genotypic features, we compared transcriptome similarity between murine pLSECs cultured in 2D HH chip and pLSECs isolated at different hepatic fibrosis stages. Notably, we observed cell morphologies of murine pLSECs resembling human LSECs under diverse mechanical conditions (Fig. 2H and fig. S2, A and C). Subsequently, pLSECs were isolated from mice with early (4W) and late (12W) fibrosis induced by carbon tetrachloride

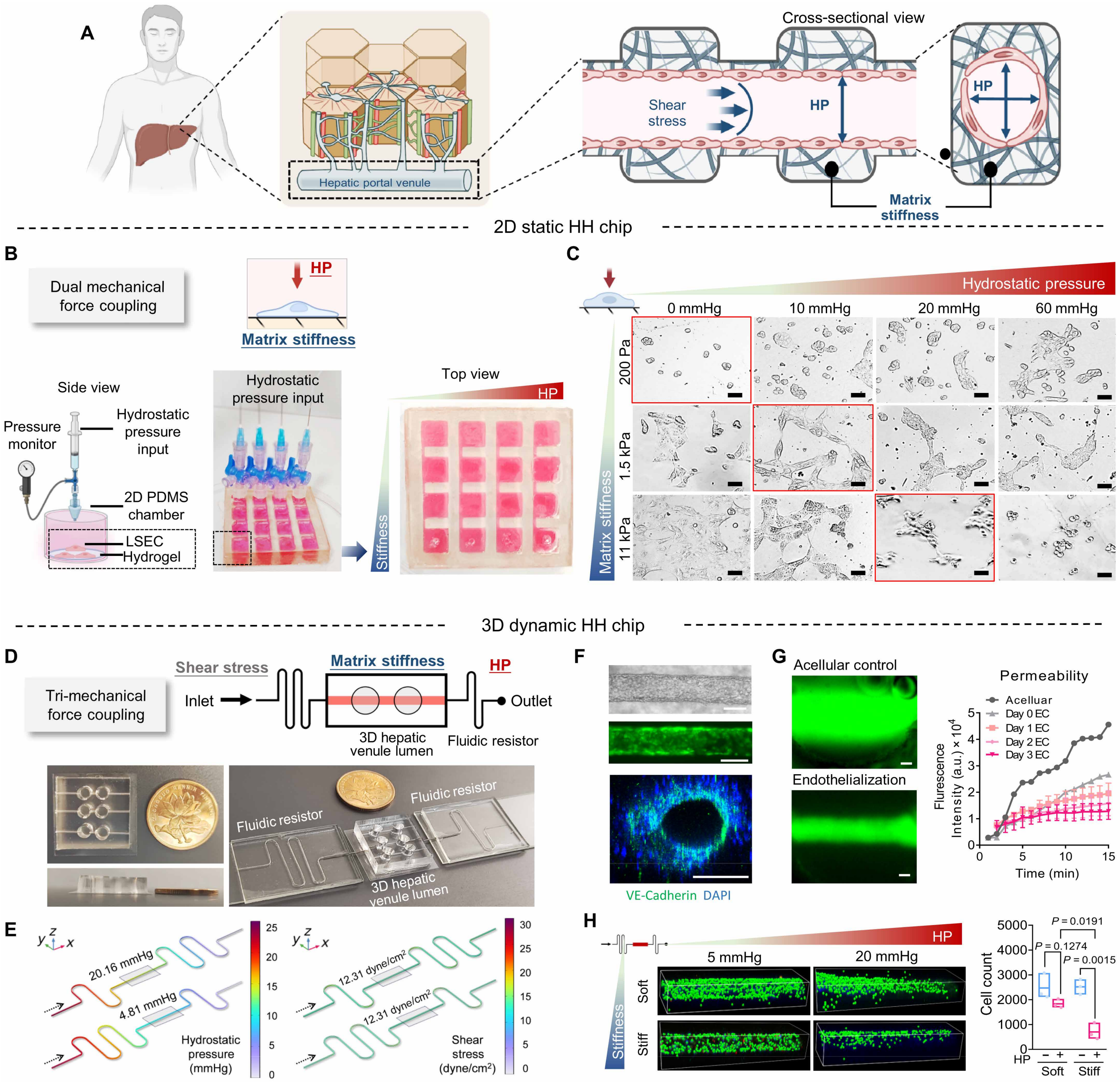

**Fig. 1. Establishment of 2D static and 3D dynamic HH chip.** (**A**) Schematic of the mechanical microenvironment in the hepatic vasculature, including HP, shear, and matrix stiffness. (**B**) Schematic of a 2D static HH chip constructed in vitro, each set of four chambers was connected to a pressure pump. (**C**) Cellular morphology of LSECs cultured on substrates with varying stiffness after a 4-hour gradient HP stimulation. Scale bars, 50 μm. (**D**) Schematic of 3D dynamic HH chip. Photographs of the 3D hepatic venule lumen connected to a fluidic resistor. (**E**) Computational fluid dynamics of shear stress and pressure within the resistors when perfusing the culture medium. (**F** and **G**) LSECs formed tubular structures (F) and vascular barrier (G) after perfusion incubation in 3D HH chip. Scale bars, 150 μm. a.u., arbitrary units. (**H**) Representative images of the nucleus of LSECs in the 3D lumen. Green dots indicate the location of cellular nuclei. Quantification of LSEC numbers in the 3D lumen (*n* = 3). Data represent means ± SEM. Statistics: two-way ANOVA with Tukey's test in (H).

($CCl_4$) for 4 and 12 weeks, respectively. RNA samples from normal mice (NC), 4W, 12W, soft substrates with low pressure (Soft + LP), and stiff substrates with high pressure (Stiff + HP) were sequenced (Fig. 2H and fig. S2A). Differentially expressed genes (DEGs) analysis revealed marked changes of LESCs during both in vivo fibrosis progression (NC versus 4W versus 12W) and in vitro culture (NC versus Soft + LP versus Stiff + HP) (fig. S2B). Comparing altered genes expression in early and late fibrosis stages, 84.9% up-regulated and 93.62% down-regulated genes in in vitro–cultured pLSECs coincided with those in early-stage fibrotic liver. Similarly, 78.63% up-regulated and 79.83% down-regulated genes in 2D cultured pLSECs mirrored changes in late-stage fibrosis (Fig. 2I).

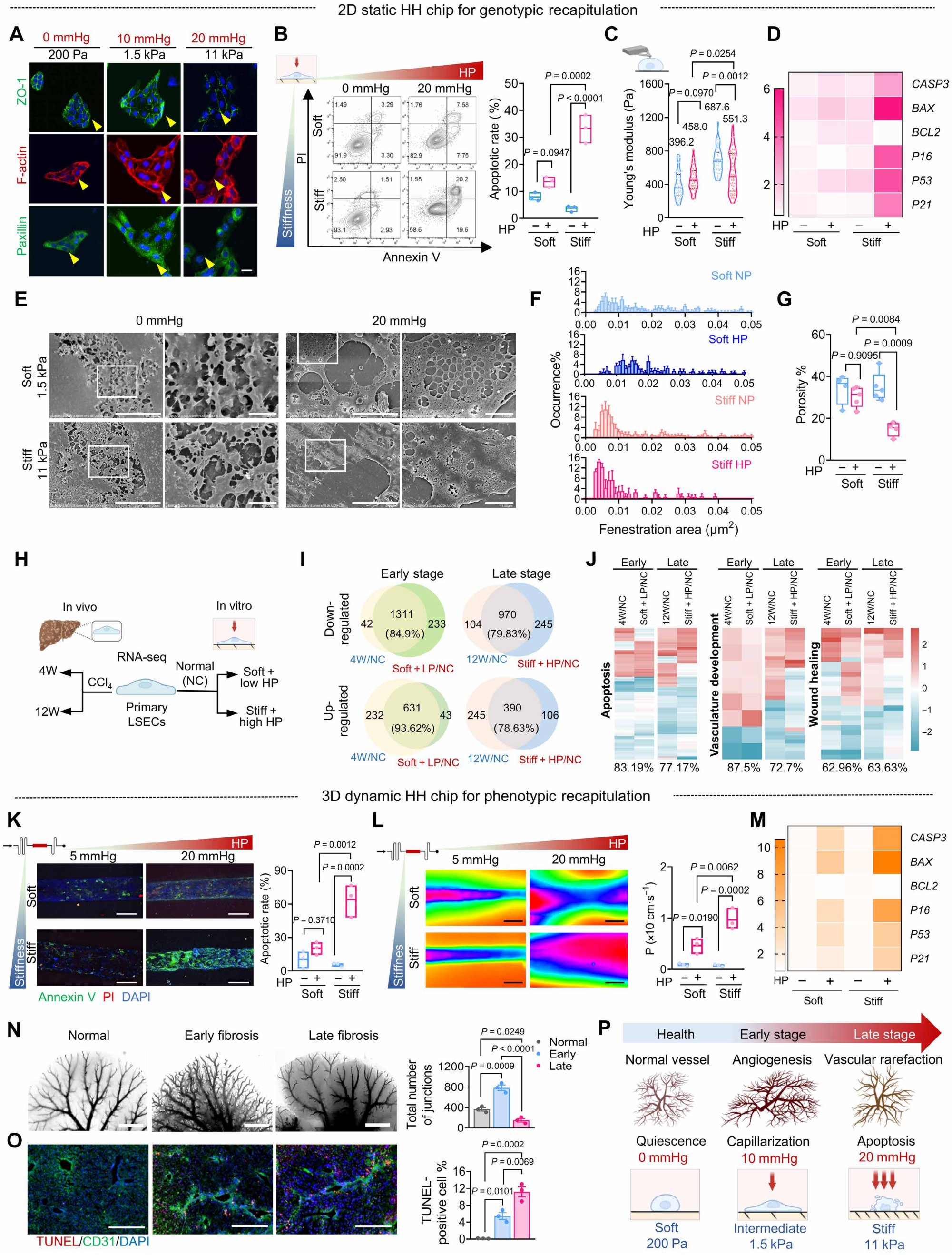

**Fig. 2. The HH chips replicate the phenotypic and genotypic features of vascular degeneration in cirrhosis.** (**A**) LSEC morphology under different mechanical forces: tight junctions (ZO-1, green), cytoskeleton (F-actin, red), and focal adhesions (paxillin, white). Scale bar, 50 μm. (**B**) Apoptosis analysis via annexin V/PI in 2D model ($n = 3$). (**C**) Young's modulus of LSECs after 4-hour HP stimulation (≥30 measurements per condition). (**D**) mRNA levels of apoptosis/senescence markers (*CASP3*, *BAX*, *BCL2*, *P16*, *P53*, and *P21*) under stiffness-HP coupling in vitro. (**E**) Scanning electron microscopy images of LSEC fenestrae. Scale bars, 1 μm after zoom. (**F** and **G**) Fenestrae area distribution and porosity under different mechanical conditions ($n \geq 4$). (**H** to **J**) Genotypic recapitulation. (H) Schematic of RNA sequencing (RNA-seq) workflow comparing in vitro (Soft + LP and Stiff + HP) and in vivo (4-/12-week fibrotic) pLSECs versus normal (NC). Aim: Characterization of the biomimetic bioengineered 2D HH chip. (I) Venn diagrams of DEG overlap in early and late-stage pLSECs (DEG defined as count of >10, $q < 0.01$, $|\log_2 FC|$ of >1). Similarity is expressed as a percentage. (J) Heatmap of DEGs related to biological processes, with similarity percentages shown. (**K**) Immunofluorescence images and quantification of apoptotic LSECs (annexin V) cultured in the 3D dynamic lumens with non–cross-linked (soft) and cross-linked (stiff) collagen (3 mg/ml; $n = 3$). Scale bars, 150 μm. (**L**) Permeability of the 3D lumen with LSECs by perfusion with dextran–fluorescein isothiocyanate (FITC; $n = 3$). Scale bars, 150 μm. (**M**) Combined effects of stiffness, HP, and shear stress on apoptosis/senescence markers. (**N** to **P**) Phenotypic recapitulation. (N) Hepatic vascular morphology at different fibrosis stage ($n = 3$). Scale bars, 5 mm. (O) Apoptotic ECs (CD31$^+$, green; and TUNEL$^+$, red) at different fibrosis stages ($n = 3$). Scale bars, 100 μm. TUNEL, terminal deoxynucleotidyl transferase–mediated deoxyuridine triphosphate nick end labeling. (P) Schematic diagram explaining the mechanism of vascular degeneration in cirrhosis, involving stiffness-dependent HP-induced EC damage. Data represent means ± SEM. Statistics: one-way analysis of variance (ANOVA) in (N) and (O); and two-way ANOVA with Tukey's test in (B), (C), (G), (K), and (L).

We further analyzed the pathways involved in modulating LSEC phenotypic changes during different fibrosis stages, focusing on overlapping genes (Fig. 2J). We compared gene expression in pathways related to cell injury (including apoptosis and cellular senescence), vascular remodeling [e.g., vasculature development; (*28*)], wound healing, mechanotransduction [e.g., cell adhesion molecules, and regulation of actin cytoskeleton; (*29*)], and vascular smooth muscle contraction, which revealed significant similarities between in vitro and in vivo counterparts (fig. S2D). Collectively, the in vitro–cultured pLSECs faithfully recapitulate their counterparts under pathological microenvironment in vivo at the genotypic transcriptome level.

### The HH chips recapitulate cirrhotic vascular phenotypic features

To assess the biomimetic accuracy of the HH chips, we analyzed the phenotypic characteristics of hepatic vessels across various stages of cirrhosis. This involved decellularization, vascular reperfusion, immunohistochemistry, and gene expression profiling, enabling a direct comparison between HH chips and fibrotic livers.

We first integrated tissue decellularization with vascular reperfusion to examine the phenotypic features (i.e., vascular morphology) in $CCl_4$-induced fibrotic murine livers (Fig. 2, K and L; and fig. S3, A and B). In early-stage fibrotic livers, an increase in vessel number and the emergence of smaller vessels were observed, indicating active angiogenesis (Fig. 2, N and O). Conversely, late-stage fibrosis was characterized by reduced vessel density, enlarged vessel diameters, and the absence of small vessels at extremities, coupled with increased collagen deposition (fig. S3F). These changes suggest that angiogenesis is intermittent and that vascular degeneration impedes the reversal of cirrhosis. Further analyses highlighted endothelial cell (EC) apoptosis and senescence, predominantly in areas associated with late fibrosis such as the portal tract and portal-to-portal bridging fibrosis region (Fig. 2O and fig. S3C). In vivo cirrhosis develops with increased tissue stiffness and portal pressure, and hepatic vasculature is in a state of vascular angiogenesis in early stages and vascular degeneration in late stages (Fig. 2P).

The HH chips successfully mimicked these dynamic phenotypic changes in hepatic vasculature by adjusting matrix stiffness and mechanical pressure (Fig. 2Q), demonstrating their potential as models for studying cirrhosis progression and therapy.

### Screening enabled by the HH chip identifies GPR116 as a potential mechanical sensor affecting EC damage

To investigate the response of liver blood vessels to HP stimulation, we implemented a three-step screening process to identify potential mechanosensors among membrane-integrated proteins that regulate this response. The primary screening involved culturing LSECs in a 2D HH Chip. Here, cells were exposed to 20-mmHg HP for durations of 0, 4, and 24 hours, followed by RNA collection for transcriptome sequencing. After 4 hours of HP treatment, cell detachment from the substrate was observed; however, the total cell number increased after 24 hours, suggesting that substrate-adhered cells might have effectively resisted the pressure stimulus and proliferated. We identified eight membrane surface protein-related genes that exhibited opposite expression trends at 4 and 24 hours of HP exposure (Fig. 3, A and B). The secondary screening involved analyzing a human liver cirrhosis single-cell sequencing dataset (GSE13610331) to identify genes specifically expressed in liver vascular ECs, with only *GPR116* emerging as specific (Fig. 3, C to E). The third step involved validation in human and murine cirrhotic liver samples (Fig. 3, F and G). We found elevated levels of GPR116 in cirrhotic tissues, primarily localized in the central vein region, fibrous bridges, and fibrous nodules (Fig. 3G). GPR116 expression was not observed in activated hepatic stellate cells (HSCs) within murine liver fibrotic tissues (fig. S4A). We found that LSECs have the highest expression levels of GPR116 among all types of cells in the liver (fig. S4B).

### GPR116 is required for HP responses in LSECs

GPR116, an adhesion GPCR (aGPCR), expressed in ECs, has demonstrated roles in vascular malformations and leakage (*30*, *31*). However, its correlation with hepatic vasculature remains unexplored. aGPCRs, with a unique GPCR proteolysis site (GPS) autoproteolytic domain and N-terminal fragment (NTF)–C-terminal fragment (CTF) structure, are highly responsive to mechanical perturbations (*32*).

To confirm GPR116 as a mechanosensor for HP, we used short hairpin RNA (shRNA)–mediated knockdown of *GPR116* in LSECs (fig. S5, B and C) and assessed cellular responses in both 2D and 3D HH chip systems (Fig. 4, A to L). In the 2D HH chip, LSECs deficient in GPR116 showed diminished apoptosis and senescence under high HP compared to control cells, suggesting reduced mechanosensitivity (Fig. 4, A to D; and fig. S5, D to F). *Gpr116* knockdown preserved fenestrae structures in pLSECs under HP (Fig. 4, F to H, and fig. S5H). In the 3D HH chip within stiff lumen, a substantial population of cells remained within the pressurized sh*GPR116*-lumen, with minimal apoptosis (Fig. 4, I to L). The integrity of the vascular barrier was maintained, demonstrating low vascular permeability in sh*GPR116*-lumen following pressure stimulation (Fig. 4K). ECs in the circulation are exposed to diverse mechanical forces, not only HP but also shear stress, stretch, and matrix stiffness (*33*). Under various mechanical stimuli, shControl and sh*GPR116* LSECs showed no significant differences in morphology or cytoskeleton structure (fig. S6, A to C). Intriguingly, HP uniquely activates GPR116 in LSECs. Although PIEZO1, PIEZO2, and TRPV4 are recognized as mechanical sensors (*34*–*36*), our study silenced these receptors in LSECs, revealing that none of them serve as HP mechanosensors in LSECs (fig. S6, D to F). These findings collectively underscore the indispensability of GPR116 in enabling LSECs to effectively respond to HP.

### GPR116 regulates vascular injury during cirrhosis

To elucidate the role of GPR116 in vascular injury, we used *Gpr116*fl/fl; *Cdh5*CreERT2 conditional knockout (KO) mice to selectively suppress GPR116 expression in ECs (Fig. 4M). In $CCl_4$-induced late-stage fibrotic KO mice, we observed a significantly reduced liver GPR116 expression (Fig. 4N). This reduction correlated with increased vascularity, decreased apoptosis among ECs, and an upregulation of genes related to vascularization (Fig. 4, O and P). DEG of late-stage hepatic ECs revealed clear distinctions between wild-type (WT) and KO mice (fig. S7, A and B). Furthermore, analysis of Kyoto Encyclopedia of Genes and Genomes (KEGG) pathways exhibited significant alteration in cytokine-cytokine receptor interaction, the Hippo signaling pathway, and phosphatidylinositol 3-kinase (PI3K)–Akt signaling (fig. S7C). In summary, our findings highlight the specific expression of GPR116 in the hepatic ECs and its critical involvement in vascular injury during cirrhosis by responding to pressure stimulation (Fig. 4Q).

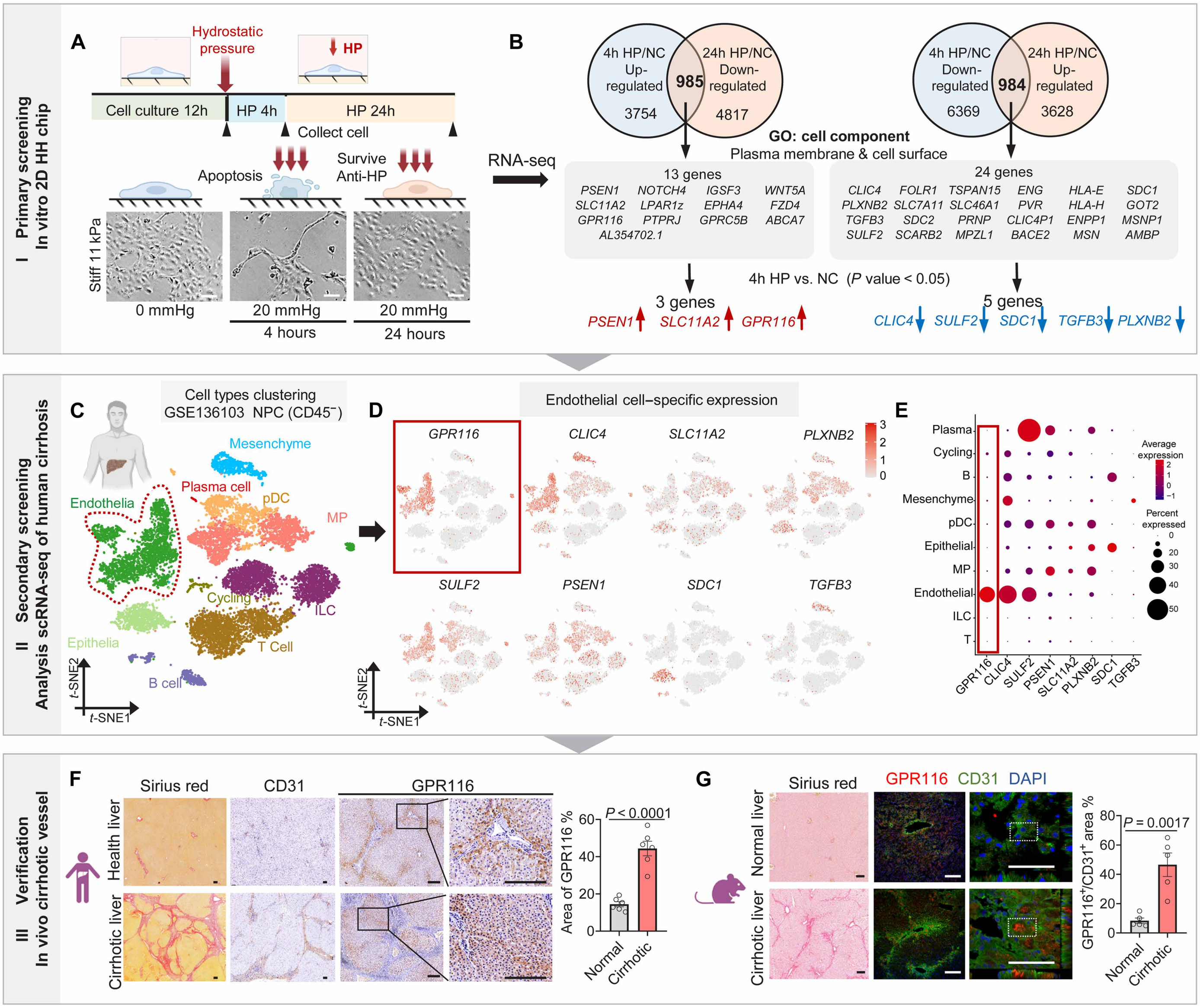

**Fig. 3. Screening enabled by the HH chip identifies GPR116 as a potential mechanical sensor affecting EC damage.** (**A** and **B**) Primary screening for potential mechanosensor responsive to HP. (A) LSECs cultured on 11-kPa substrates under 20-mmHg HP (0, 4, and 24 hours). RNA-seq performed at each time point. (B) Venn diagrams of DEGs trends of 4 and 24 hours HP-treated LSECs (4h HP and 24h HP), as compared to those of non–HP-treated LSECs (NC). The overlapping up/down-regulated genes (count > 10; FC versus NC) were filtered by plasma membrane/cell surface GO terms. Candidate genes ($P < 0.05$ in 4h HP/NC) were labeled (red, up-regulated; and blue, down-regulated). (**C** to **E**) Secondary screening analyzed the human single-cell sequencing dataset GSE136103 to pinpoint genes uniquely expressed in ECs. (C) Cell-type clustering based on CD45$^-$ of the dataset. (D) Expressions of *GPR116*, *CLIC4*, *SULF2*, *PSEN1*, *SLC11A2*, *PLXNB2*, *SDC1*, and *TGFB3* in 10 clusters. (E) Dot plot of selected gene expression in different cell types. pDC, plasmacytoid dendritic cell; ILC, innate lymphoid cell; t-SNE, t-distributed stochastic neighbor embedding. (**F** and **G**) Validation of GPR116 expression in cirrhotic liver vasculature in humans and mice. (F) Representative images of Sirius Red, CD31, and GPR116 staining in human normal and cirrhotic liver samples. Quantification of the area percentage of GPR116 ($n = 6$). Scale bars, 150 μm. (G) Representative immunofluorescence images of GPR116 and CD31 costaining of in liver. Scale bars, 100 μm. Quantification of the percentage area of GPR116 in CD31$^+$ ECs ($n = 5$). Data represent means ± SEM. Statistics: two-tailed unpaired *t* test in (F) and (G).

## Mechanosensing of GPR116 by HP

To elucidate the response of GPR116 to HP, we measured intracellular cyclic adenosine 3′,5′-monophosphate (cAMP) levels in cells before and after HP exposure. HP stimulation increased cAMP accumulation in LSECs (Fig. 5A) and enhanced mini–G protein signaling in human embryonic kidney (HEK) 293T cells expressing full-length GPR116 (Fig. 5B). The stachel peptide, however, did not affect cAMP or mini–G signaling, supporting evidence that it activates GPR116 via Gαq rather than Gαs (*37*). Conversely, *GPR116* knockdown inhibited the increases in cAMP induced by HP (Fig. 5A), suggesting that GPR116 mediates HP-induced apoptosis through Gαs activation.

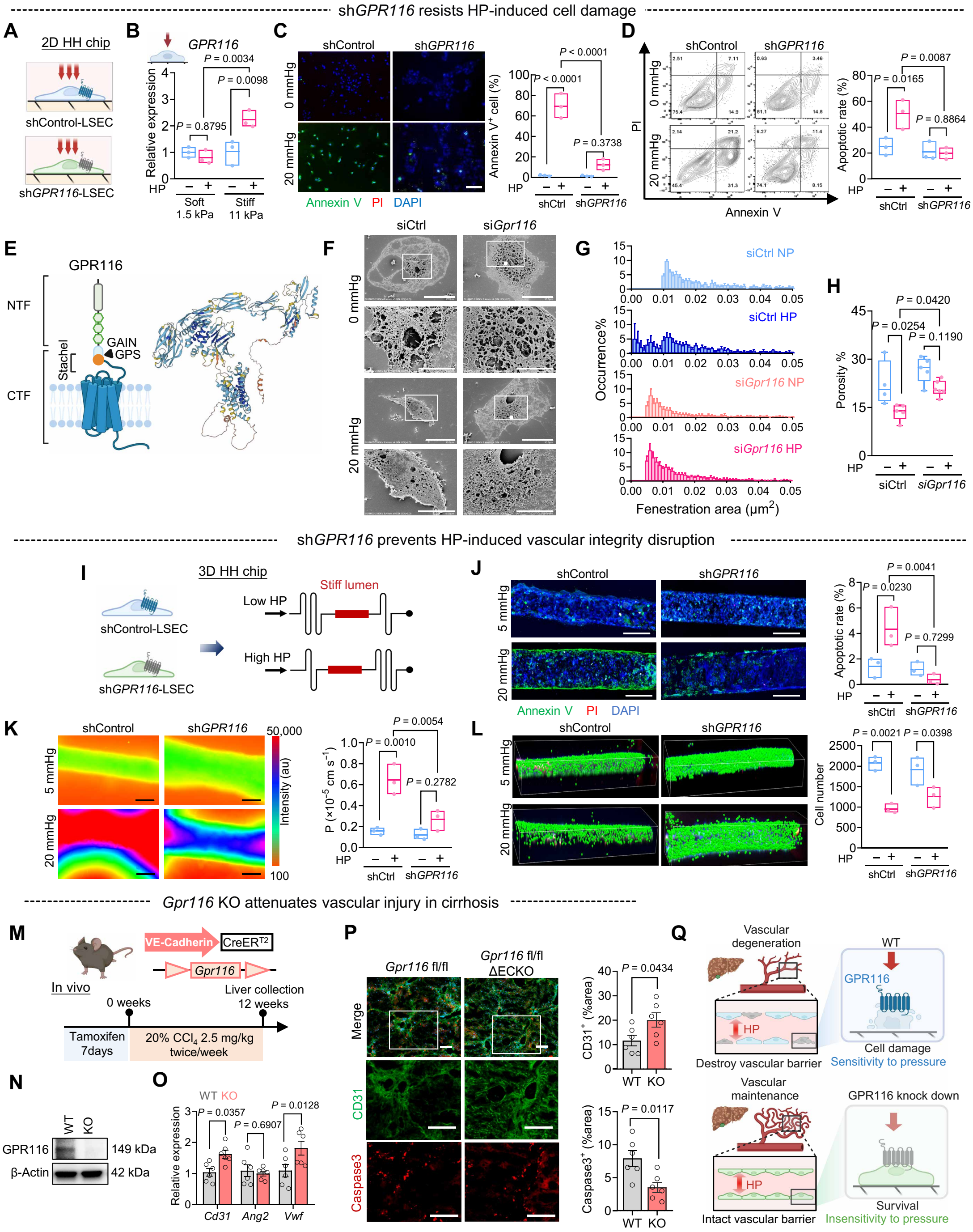

**Fig. 4. GPR116 mediates LSEC responses to HP in HH chips and cirrhotic models.** (**A**) Schematic of HP applied to shControl and sh*GPR116* LSECs in 2D static HP chamber. (**B**) Relative mRNA levels of *GPR116* in LSECs cultured in a 2D HP chamber ($n = 3$). (**C** and **D**) Apoptosis in shControl/shGPR116 LSECs (11 kPa ± HP, 4 hours): Immunofluorescence images (C) and flow cytometry (D) ($n = 3$). Scale bar, 100 μm. (**E**) The Alphafold2-predicted and illustrative protein structure of GPR116. Created in BioRender: D. Lab (2025); https://BioRender.com/j61i791. (**F**) Scanning electron microscopy of pLSEC fenestrae (si*Gpr116* and siCtrl) under stiff substrate (11 kPa) +20-mmHg HP. Scale bars, 1 μm, zoom. (**G** and **H**) Fenestrae area distribution (G) and porosity (H) ($n \geq 3$). (**I**) Schematic of HP applied to shControl and sh*GPR116* LSECs within the 3D dynamic HP lumens. (**J**) Apoptosis in shControl and sh*GPR116* LSECs cultured in a 3D dynamic stiff lumen ($n = 3$). Scale bars, 150 μm. (**K**) Permeability of the 3D lumen with shControl and sh*GPR116* LSECs perfused with dextran-FITC ($n = 3$). Scale bars, 150 μm. a.u., arbitrary units. (**L**) Nuclei of LSECs in the 3D lumen. Green dots indicate the location of cellular nuclei ($n = 3$). (**M**) Schematic of liver samples harvested for characterization using conditional knockout (KO) mice *Gpr116*fl/fl *Cdh5*CreERT2 injected with tamoxifen followed by $CCl_4$ induction. (**N**) Western blot analysis of GPR116 expression in fibrotic liver tissue. (**O**) mRNA level of *Cd31*, *Ang2*, and *Vwf* in liver tissue from wild-type (WT) and KO mice ($n = 6$). (**P**) Immunofluorescence images and quantification of CD31 and Caspase3 costaining in cirrhotic liver from WT and KO mice ($n = 6$). Scale bars, 100 μm. (**Q**) Schematic of GPR116 responding to HP effect on hepatic vascular injury during cirrhosis progression. Created in BioRender: D. Lab (2025); https://BioRender.com/j61i791. Data represent means ± SEM. Statistics: two-way ANOVA with Tukey's test in (B), (C), (D), (H), (J), (K), (L), and (O); and two-tailed unpaired *t* test in (P).

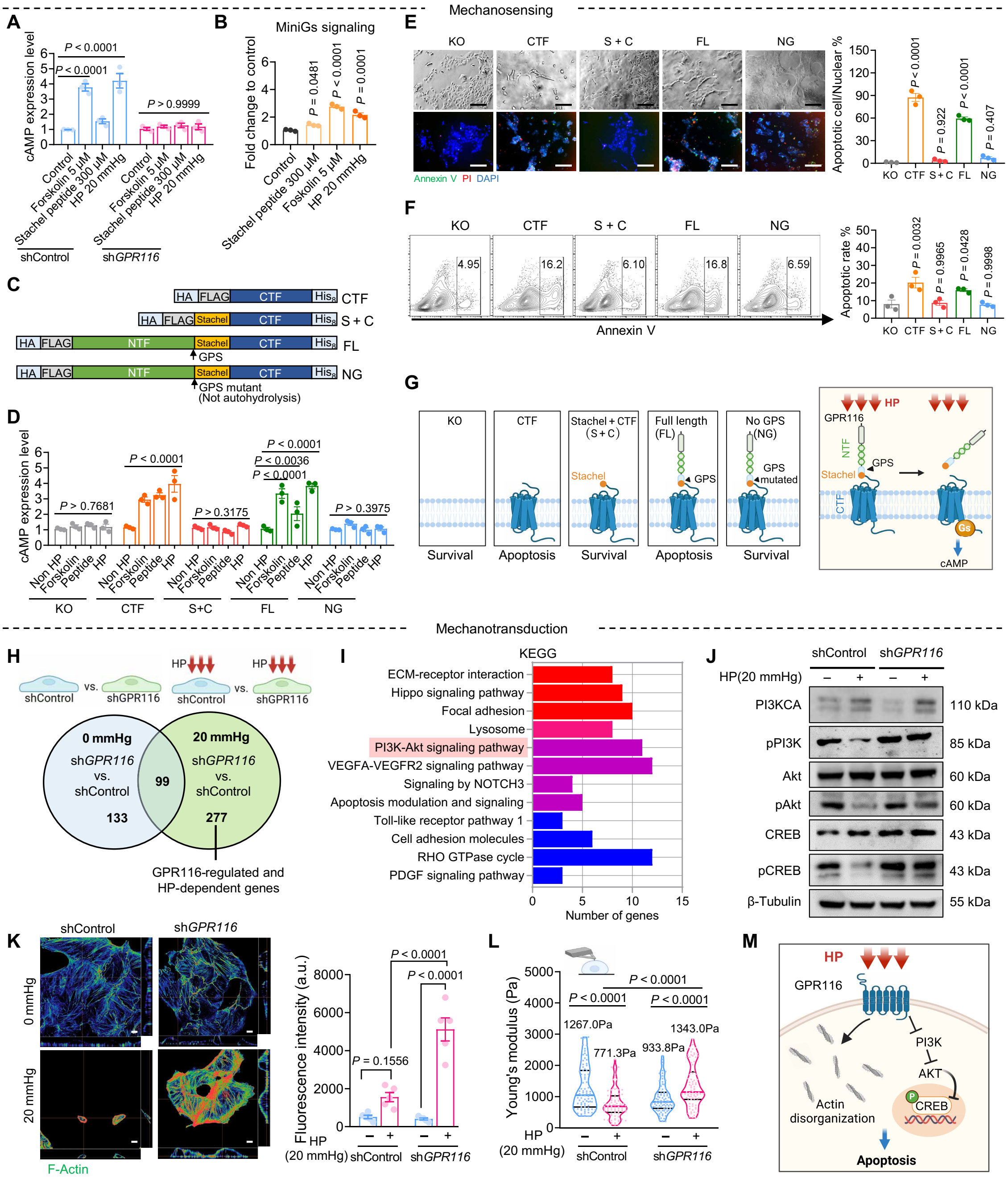

**Fig. 5. Mechanosensing and mechanotransduction of GPR116 response to HP.** (**A** to **G**) Mechanosensing of GPR116 response to HP. (A) Relative intracellular cAMP levels in shControl/sh*GPR116* LSECs after stimulation with forskolin, stachel peptide, and 20-mmHg HP, normalized to untreated shControl LSECs ($n = 3$). (B) Relative mini Gs signaling levels in HEK293T cells overexpressing full-length GPR116 after stimulation ($n = 3$). (C) Schematic of GPR116 mutants' overexpression in CRISPR-KO LSECs: CTF (C-terminal fragment), S + C (CTF + stachel peptide), FL (full-length), and NG (noncleavable FL). (D) Relative intracellular cAMP levels in LSECs overexpressing GPR116 mutants. Data normalized to untreated KO LSECs ($n = 3$). (E and F) Cell morphology and apoptosis in LSECs overexpressing *GPR116* mutants on 11 kPa ± HP. (E) In situ staining results ($n = 3$). Scale bar, 100 μm. (F) Flow cytometry analysis results ($n = 3$). (G) Schematic of GPR116 mutants and the mechanism by which GPR116 senses HP via GPS hydrolysis, inducing Gs activation and cAMP accumulation. Created in BioRender: D. Lab (2025); https://BioRender.com/j61i791. (**H** to **M**) Mechanotransduction pathway of GPR116 responds to HP to regulate cell apoptosis. (H) Venn diagrams of DEGs in sh*GPR116*-LSECs ± HP compared to those in shControl LSECs show 227 DEGs are *GPR116* regulated and dependent on HP (DEG defined as count of >10, $q < 0.01$, $|\log_2 FC|$ of >1). (I) KEGG pathway analysis of the 277 DEGs. GTPase, guanosine triphosphatase; PDGF, platelet-derived growth factor. (J) Western blot results of PI3K/Akt/CREB phosphorylation (β-tubulin control) in LSECs with/without HP treatment. (K) F-actin fluorescence intensity in LSECs with/without HP treatment ($n = 5$). a.u., arbitrary units. Scale bars, 10 μm. (L) Young's modulus of LSECs after HP exposure. (M) Schematic of GPR116 mechanotransduction pathway. GPR116 transduces mechanical force signals of HP intracellularly, leading to cell apoptosis by promoting cytoskeletal disorganization, inhibiting activation of the PI3K-Akt signaling pathway, and suppressing CREB phosphorylation. Created in BioRender: D. Lab (2025); https://BioRender.com/j61i791. Data represent means ± SEM. Statistics: two-way ANOVA in (B), (D), (K), and (L); and one-way ANOVA in (A), (E), and (F).

GPR116, an aGPCR, contains a proteolytic site (GPS) in its extensive extracellular N-terminal domain, facilitating autocatalytic cleavage that activates downstream signaling through the exposed stachel ligand (*38*). Three activation pathways have been identified: direct stimulation by agonist peptides, N terminus binding to ECM components, and activation through mechanical stimulation (*39*).

To investigate how GPR116 senses HP, we used CRISPR-Cas9 to generate GPR116 KO LSECs and overexpressed various GPR116 constructs, including the CTF, CTF with stachel peptide (S + C), full-length (FL), and a hydrolysis-resistant full-length variant (NG) resulting from a GPS mutation (Fig. 5C and fig. S5G). Our data revealed that S + C and NG were insensitive to HP, showing no change in cAMP levels or apoptosis. In contrast, CTF exhibited similar responses to FL, indicating HP sensitivity mediated by cAMP and apoptosis (Fig. 5, D to F). This suggests that HP-induced GPR116 activation is primarily driven by GPS autohydrolysis (Fig. 5G). These results highlighted the distinct role of GPR116 in sensing specific mechanical force in LSECs.

### Mechanotransduction pathway of GPR116 in HP-induced apoptosis

To explore how GPR116 transduces mechanical signals from HP into cellular responses and regulates apoptosis, we compared the DEGs between shControl and sh*GPR116* LSECs under both HP-stimulated and untreated conditions. After excluding 99 overlapping genes, we identified 277 DEGs specifically regulated by GPR116 and responsive to HP (Fig. 5H). KEGG pathway enrichment analysis revealed that these genes were primarily involved in ECM-receptor interaction, the Hippo signaling pathway, focal adhesion, and the PI3K-Akt signaling pathway (Fig. 5I). The PI3K-Akt pathway, critical for cell survival (*40*), activates Akt, which, in turn, phosphorylates cAMP response element–binding protein (CREB) (*41*), enhancing its transcriptional activity and inhibiting apoptosis (*42*). We found that sh*GPR116* LSECs exhibited higher levels of Akt and CREB phosphorylation after HP treatment compared to shControl LSECs (Fig. 5J).

By characterizing changes in the fenestrae structure, cytoskeleton, and cellular stiffness, we found that control group LSECs exhibited apoptosis, decreased fenestrae porosity, cytoskeleton disassembly, decreased nuclear volume, and decreased cellular stiffness after HP stimulation. In contrast, knockdown *GPR116* LSECs not only survived but also showed intact fenestrae structure, cytoskeletal remodeling, increased nuclear volume, and enhanced cellular stiffness after HP treatment (Figs. 4, F to H, and 5, K and L; and fig. S5F). These observations indicate that GPR116 modulates EC responses to mechanical stress by orchestrating cytoskeletal reorganization and maintaining the integrity of fenestrae structure.

Collectively, our findings demonstrate that GPR116 mediates the transduction of mechanical forces from HP into cellular responses, primarily by modulating cytoskeletal dynamics, which, in turn, influences the PI3K-Akt signaling pathway and CREB phosphorylation, thereby affecting apoptosis (Fig. 5M).

### EC therapy of cirrhosis by targeting GPR116 to prevent vascular degeneration

In the HH chips, we observed that inhibition of GPR116 in LSECs effectively resisted HP-induced cellular damage. We then investigated whether supplementation of anti-HP shGPR116-LSECs into cirrhotic livers could ameliorate cirrhosis by preventing vascular degeneration. To assess the efficacy of EC therapy targeting GPR116 in treating cirrhosis, we transplanted LSECs into late-stage livers via intrasplenic injection (Fig. 6A). Bioluminescent tracking of Akaluc-transfected sh*GPR116* LSECs showed sustained signals for 3 weeks in both healthy and cirrhotic mice (Fig. 6B). In vivo, sh*GPR116* LSECs contributed to reducing collagen deposition and showed trends toward attenuating HSC activation and enhancing vascularization compared to controls (Fig. 6, C to E). These results highlighted the therapeutic potential of GPR116 inhibition in LSECs to sustain LSEC survival and mitigate cirrhosis progression.

### Gene therapy of cirrhosis by targeting GPR116 to prevent vascular degeneration

The adeno-associated virus (AAV) system has demonstrated safety and stability in gene delivery and expression over time. To explore the effectiveness of gene therapy strategies targeting GPR116 for the treatment of cirrhosis, we used AAV2/9 vector to deliver shRNA to suppress GPR116 expression (Fig. 6G). We administered either AAV2/9-*Gpr116* shRNA or a control (AAV2/9-Ctrl shRNA) via intravenous injection, with the AAV began to exert its potent effects ~3 weeks postinjection.

To determine the effect of *Gpr116* inhibition on delaying the fibrosis progression, AAV2/9-*Gpr116* shRNA was administered in mice at early-stage liver fibrosis, followed by 8 weeks of $CCl_4$ induction to advanced fibrosis (Fig. 6F). Results indicated a decrease in GPR116 expression in the liver, which correlated with improved vascularization and reduced collagen deposition (Fig. 6, H to J). This suggested that initiating inhibition of GPR116 at an early stage can mitigate vascular degeneration, thus impeding fibrosis progression.

## DISCUSSION

Our study introduced the "hepatic hypertension on-a-chip" (HH chip) model, an MPS meticulously designed to replicate the complex hemodynamic and matrix environments of the cirrhotic liver. The HH chips illuminated the role of matrix stiffness in promoting EC injury under elevated pressure. Notably, our HH chips identified GPR116 as an essential mechanosensor in LSECs, pivotal in regulating vascular endothelial cellular responses to abnormal HP in cirrhosis. This discovery sheds light on aspects of mechanotransduction pathways in liver pathology and suggests potential therapeutic approaches for managing cirrhosis.

Traditional in vitro biomechanical models mainly affect cell morphology and function by modulating substrate stiffness under 2D static culture conditions (*6*, *43*) or stimulate cells by applying stable shear force or pressure under 2D dynamic culture conditions (*12*, *44*). Many 3D models developed in recent years, which mainly mimic the structure of the in vivo microenvironment (*45*–*47*), are unable to accurately replicate both the hemodynamic and matrix environments of cirrhosis and to reproduce pathological features such as modeling angiogenesis in early fibrosis and vascular degeneration in advanced stage (*2*, *48*). Our HH chip addresses this gap, integrating and decoupling HP, shear stress, and matrix stiffness to provide a controlled, reproducible environment for in-depth study of cirrhotic pathology. The pathophysiological relevance of our findings is underscored by the ability of the HH chip to simulate the complex interplay between mechanical forces and the ECs in cirrhosis.

We combined MPS and human cirrhotic single-cell sequence databases to screen for effective proteins, identifying GPR116 as a

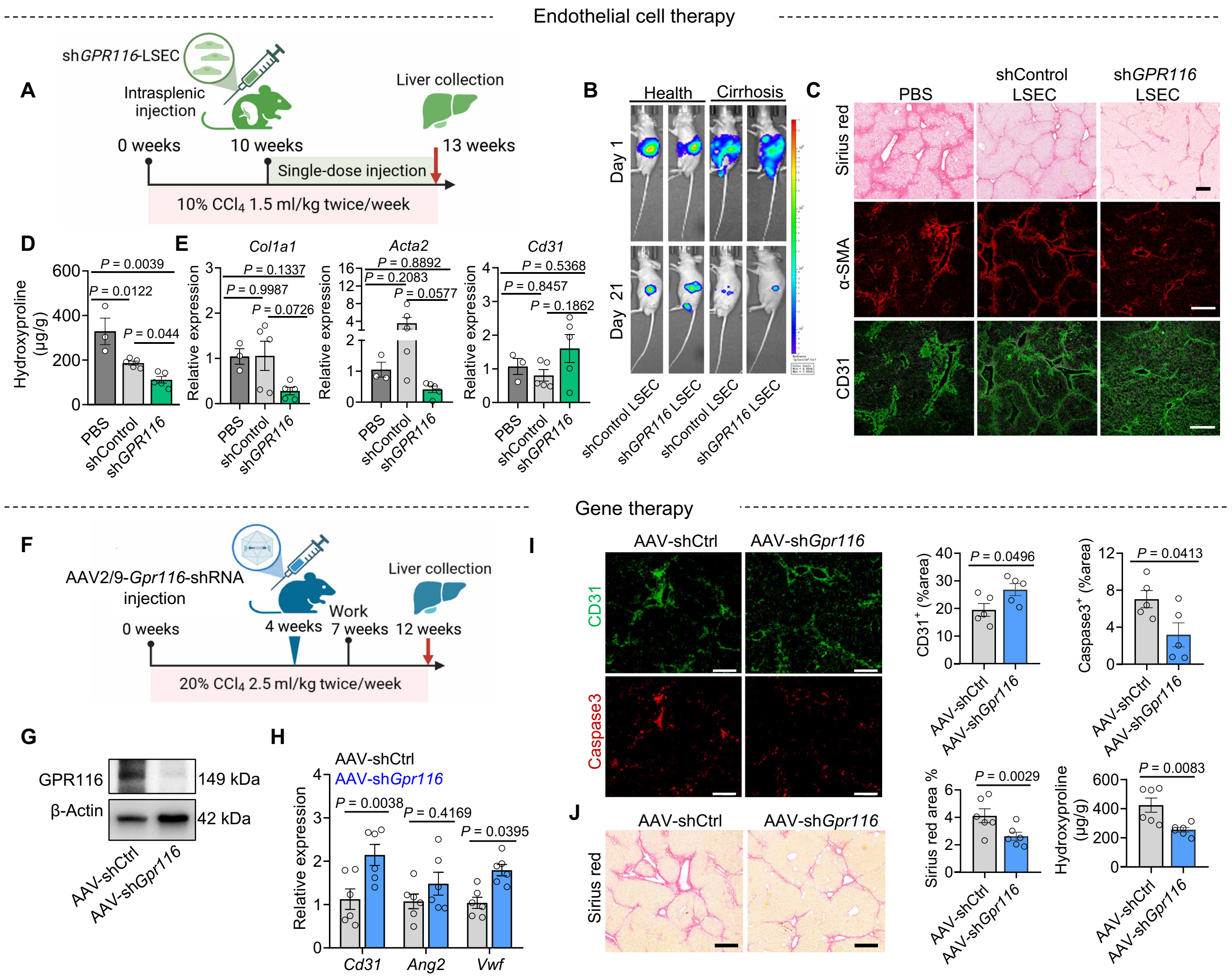

**Fig. 6. Treatment of cirrhosis by targeting GPR116 to prevent vascular degeneration.** (**A**) Schematic of late-stage liver fibrosis induction in BALB/C nude mice and LSECs transplantations via intrasplenic injection. (**B**) Bioluminescent signal of LSECs-Akaluc in vivo after systemic administration for 1 and 21 days. (**C**) Representative images of Sirius Red staining of livers from PBS, shControl, and sh*GPR116* LSECs transplantation group. Immunofluorescent staining for α–smooth muscle actin (red) and CD31 (green) of livers from different groups. Scale bars, 100 μm. (**D** and **E**) Transplantation effects of LSECs were evaluated by hydroxyproline quantification and the relative mRNA expression of *Col1a1*, *Acta2*, and *Cd31* in liver tissues. PBS group, $n = 3$; shControl, $n = 5$; and sh*GPR116*, $n = 5$. (**F**) Schematic of AAV2/9-*Gpr116*-shRNA administered via the tail vein at the $CCl_4$-induced early-stage liver fibrosis and collection of liver samples at 12 weeks. (**G**) Western blot analysis of GPR116 expression in fibrotic liver tissue. (**H**) Quantification of the relative mRNA expression of *Gpr116*, *Cd31*, *Ang2*, and *Vwf* in liver tissue from the AAV-shControl and AAV-sh*Gpr116* groups ($n = 6$). (**I**) Representative immunofluorescence images of CD31 and Caspase3 costaining of liver from AAV-shControl and AAV-sh*Gpr116* group. Scale bars, 100 μm. The right side is quantification of the area percentage of CD31 and Caspase3 ($n = 5$). (**J**) Representative images of Sirius Red staining of liver from the AAV-shControl and AAV-sh*Gpr116* groups. The middle side is quantification of the Sirius Red area. The right side is hydroxyproline quantification ($n = 6$). Data are means ± SEM. Statistics: two-way ANOVA with Tukey's test in (H); one-way ANOVA with Tukey's test in (D) and (E); and two-tailed unpaired *t* test in (G), (I), and (J).

crucial player in sensing HP and regulating vascular injury. By combining MPS with publicly available databases of biological samples (genomics, proteomics, etc.), we can systematically screen and pinpoint potential biomedical targets, enhancing the accuracy and efficiency of target discovery.

To classify a protein as a mechanosensor, it ideally should meet several criteria: expression in relevant cells, essentiality for immediate cellular signaling in response to relevant forces, and activation by these forces when expressed in heterologous cells or reconstituted in lipid bilayers (*49*). Through screening with a 2D HH chip, we identified GPR116 as a mechanosensor of HP by the following evidences: (i) GPR116 is specifically expressed in liver ECs; (ii) GPR116 is involved in sensing HP, triggering GPS autohydrolysis and activation of Gs signaling. It transduces these mechanical signals into the cytosol and regulates apoptosis by promoting cytoskeletal disorganization and inhibiting the activation of the PI3K-Akt signaling pathway, as well as the phosphorylation of CREB. However, GPR116 does not respond to shear stress, stretch, or changes in matrix stiffness (fig. S6, A to C), highlighting its specificity to HP; (iii) Overexpression of full-length human GPR116 in LSECs or HEK293T cells also activates downstream signaling pathways when exposed to pressure. Notably, GPR116 knockdown prevents HP-induced cell damage, unlike other mechanosensors such as PIEZO1, PIEZO2, and TRPV4 (fig. S6, D to F). The role of GPR116 in mediating the response of LSECs to increased HP provides insight into the pathogenesis of vascular injuries in cirrhosis.

The potential therapeutic implications of our findings extend beyond traditional antiangiogenic approaches, which are effective in early fibrosis but less so as the disease progresses to cirrhosis (*4*–*6*). Our results proposed a shift toward therapies aimed at vascular maintenance and preventing degeneration. Silencing GPR116 protected hepatic ECs from HP-induced damage, vascular barrier disruption, and maintained vascular density (Fig. 4P), suggesting it as a target for cirrhosis intervention. Nonselective beta-blockers, such as propranolol and carvedilol, effectively lower portal pressure but carry risks of hypotension and increased mortality (*50*). GPR116 is an orphan receptor that does not regulate vasoconstriction and vasodilation like adrenoceptor. Therefore, GPR116 may provide a safer alternative to alleviating portal hypertension by improving endothelial function. Supplementation with sh*GPR116* LSECs, resistant to damage from high stiffness and pressure, has alleviated cirrhosis (Fig. 6, A to C), supporting an EC-based therapeutic approach. Increasing evidence suggested that AAV-mediated gene therapy has broad therapeutic potential in various liver fibrosis models (*51*). Administering *Gpr116* shRNA via AAV injection at early stage mitigated late-stage fibrosis and inhibited vascular degeneration (Fig. 6, F to J), providing guidance for targeting mechanosensors and developing gene therapies to reverse or delay cirrhosis and reduce mortality.

Moreover, the broader relevance of matrix stiffness–dependent HP-induced EC injury suggests that similar mechanisms may contribute to vascular degeneration in other organs. The HH chip has recreated the in vivo mechanical microenvironment to model cellular pathological responses more precisely, enabling an unbiased search for mechanosensitive proteins and signaling pathways. In pulmonary hypertension research, it can mimic pathological changes in the pulmonary artery, such as alterations in the vascular wall and matrix, to observe EC abnormalities, pinpoint disease causes, and uncover potential drug targets. For atherosclerosis, it replicates plaque formation due to vascular wall damage, lipid deposition, and smooth muscle cell proliferation, revealing how mechanical stress affects lipid metabolism and inflammation and opening doors for drug or material development. In hypertensive retinopathy, it accurately simulates microvascular lesions, clarifying molecular mechanisms like cell apoptosis and barrier damage, providing biomarkers for early diagnosis and informing intervention strategies. In hypertensive nephropathy, it simulates renal microvascular hardening and identifies molecular changes in renal cells caused by mechanical pressure, spurring the development of targeted renal vascular protection and renal function repair programs. Overall, the HH chip serves as a versatile platform for modeling vascular diseases across various organs, uncovering crucial mechanisms and expediting the discovery of treatments.

In conclusion, our study highlights the HH chip as a MPS for dissecting the molecular and cellular mechanisms of cirrhosis and identifies GPR116 as a therapeutic target. Future research should focus on optimizing these therapeutic strategies and exploring the broader applicability of the HH chip in other forms of vascular injury associated with different pathological conditions. This comprehensive approach not only provides a detailed examination of how mechanical stressors like HP affect LSECs but also extends the applicability of our findings to even broader physiological and pathological contexts. Moreover, the HH chip can accelerate pathological investigation, target identification, and drug screening for hypertension-related diseases.

## MATERIALS AND METHODS

### Experimental model and study participant details

#### *Cell culture and primary cell isolation*

Human LSECs were provided by the laboratory of L. Zhang (Tsinghua University, Beijing, China), which were bought from ScienCell. The acquirement and characterization of LSECs were performed in the previous research (*6*). LSECs and human embryonic kidney cell line (HEK293T) were cultivated in Dulbecco's modified Eagle's medium (DMEM; Wisent, 319-051-CL), supplemented with 10% fetal bovine serum (FBS; Wisent, 086–150) and 1% penicillin and streptomycin (PS; Wisent, 450-201). Human umbilical cord ECs (HUVECs) were purchased from China Center for Type Culture Collection. pLSECs were isolated from C57BL/6 mice. HUVECs and pLSECs were cultured in EC medium containing 5% FBS, 1% PS, and 1% EC growth supplements (ScienCell, SC-1001-prf). All the cells were cultured at 37°C in a humidified atmosphere of 5% $CO_2$ in air.

#### *Animals*

C57BL/6 male mice (8-week-old) and Balb/c nude mice were purchased from the Laboratory Animal Resources Centre at Tsinghua University and housed in the specific-pathogen free animal facility. *Gpr116*fl/fl mice (catalog no. NM-CKO-00095) and *Cdh5*-2A-CreERT2 (catalog no. NM-KI-200173) were purchased from SHANGHAI MODEL ORGANISMS (Shanghai). *Cdh5*CreERT *Gpr116*flox mice were treated by intraperitoneal injection with tamoxifen (25 mg/ml) dissolved in corn oil (75 mg/kg of body weight). Conditional deletion of Gpr116 in mouse ECs was induced by injection of tamoxifen for 7 consecutive days.

For the $CCl_4$-induced liver fibrosis model, 8-week-old male C57BL/6 mice were treated with $CCl_4$ (2.5 ml/kg of body weight; 1:4 diluted with olive oil) by intraperitoneal injection for 4 weeks (early-stage fibrosis) or 12 weeks (late-stage fibrosis). Eight-week-old nude male mice were intraperitoneally injected with $CCl_4$ (1.5 ml/kg, 1:9 diluted with olive oil) twice a week for 10 weeks (late-stage fibrosis). All animal experiments described in this study were conducted in accordance with the guidelines and approved by the Institutional Animal Care and Use Committee of Tsinghua University and the Animal Welfare and Ethics Committee of Tsinghua University (project no. THU-02-2024-0105A).

#### *Human liver sample*

The human liver tissues from patients provided by the Department of Hepatobiliary Surgery, First Affiliated Hospital of Kunming Medical University and approved by the Institutional Review Board of Tsinghua University (project no. 20230160). Informed consent was obtained from participants. The normal and cirrhotic liver tissue specimens were obtained from distant noncancerous tissues of hepatocellular carcinoma patients who underwent hepatectomy. The extent of liver cirrhosis was verified by Sirius Red staining ($n = 6$).

## Method details

### *In vivo experiments*

*Decellularization of the liver and vascular morphology characterization*. Following the administration of Avertin anesthesia to the mice, the abdominal cavity was carefully opened using scissors to expose the liver and locate the inferior vena cava (IVC). An indwelling needle was then inserted into the IVC, and, upon confirming the blood return, a peristaltic pump was connected to perfuse the mice with a solution of 0.5 mM EDTA in phosphate-buffered saline (PBS) at a rate of 5 ml/min for 10 min. Subsequently, the mice underwent perfusion with 0.01% SDS for 1 hour, 0.05% SDS for 2 hours, and 0.1% SDS for 24 hours. Upon completing the perfusion, fast-drying ink (Deli) was gradually injected using a 1-ml syringe connected to the indwelling needle. Whole-liver morphology was captured using a DSLR camera, while liver vessel morphology was documented using a surface light imager. Additionally, vessel end morphology was photographed using a Nikon microscope at ×4 and ×10 magnifications. The data were then subjected to analysis using ImageJ software, encompassing vessel number, vessel branching, and vessel diameter statistics.

*Isolation of pLSECs*. pLSECs were isolated from C57BL/6 mice via a modified in situ collagenase digestion method through the portal vein (*6*). The liver was perfused and was digested with collagenase IV (Gibco, 17104019) and pronase (Roche, 11459643001). Hepatocytes were removed through centrifugation at 50*g*. Nonparenchymal cells were further centrifuged at 500*g* for 8 min at 4°C. The resulting pellet was resuspended in RPMI 1640 medium (Wisent, 350-030-CL) and subjected to a 25%/50% Percoll (Solarbio, P8370) gradient centrifugation at 1200*g* for 20 min. The interface containing Kupffer cells and LSECs was collected and incubated in acid-washed glass petri dishes at 37°C for 15 min. Nonadherent LSECs were collected, replated, and cultured. After 1 hour, the medium was changed to remove unattached cells. LSECs from fibrotic mice (4 and 12 weeks of $CCl_4$ induction) were directly harvested using TRIzol (Vazyme, R401-0) reagent after 2 hours. Mouse pLSECs were characterized using CD31, LYVE-1, and CD32b staining.

*AAV-infected mice*. AAV vector–mediated knockdown of mouse *Gpr116* and scrambled control were constructed, amplified, and purified by Obio Technology (Shanghai, China). AAV2/9 was injected into mice at different stages of $CCl_4$-induced hepatic fibrosis via tail vein to deliver shRNA (GCAATGTGACATTGGGATTT) that can knock down mouse Gpr116 or scramble shRNA (CCTAAGGTTAAGTCGCCCTCG). Each mouse was treated with 100 μl of sterile saline diluted with a titer of $5 \times 10^{11}$ Vector Genomes (Vg)/μl of viral genome. Mice were monitored for changes in body weight during the study. After a period of 3 weeks postinjection, serum samples were collected to assess liver function impairment, and the expression of *Gpr116* in the liver was analyzed using immunofluorescence and quantitative polymerase chain reaction (qPCR). Mice were euthanized at various stages of liver fibrosis and tissues were dissected for further analysis.

*Transplantation of EC in vivo*. For single-dose LSECs transplantation, shControl LSECs and sh*GPR116* LSECs expressing the bioluminescent enzyme Akaluciferase (Akaluc) were injected intrasplenically with PBS into mice with advanced liver fibrosis after 10 weeks of $CCl_4$ induction. The twice weekly $CCl_4$ induction was maintained even after the injection of the cells. Mice were euthanized on days 21 postinjection, and livers were harvested for analysis.

For tracking LSEC residency and survival in vivo, LSECs were engineered to stably express mVenus and Akaluc by lentiviral-mediated gene transfer, resulting in LSEC-Akaluc. For lentiviral production, the plasmid vectors pVSV-G, pΔ8.9, and pLV-CMV-mVenus-Akaluc were used in a 1:2:3 ratio. They were diluted and mixed with opti-MEM, followed by the addition of Neofect (Neofect biotech). Successful cell infection was achieved by flow sorting (BD Influx) after 48 hours.

For intrasplenic injection, BalB/C nude mice were anesthetized with isoflurane and placed on their left side to expose the splenic area. A small incision ~0.5 cm was carefully made in the tunica albuginea and basement membrane to access to one end of the spleen. Subsequently, 100 μl of $4 \times 10^5$ LSEC-Akaluc cells were injected into the spleen at a rate of 50 μl/min using a peristaltic pump. To prevent coagulation during the injection, heparin (400 U/kg) was added to the cell mixture. After cell injection, a 10-s pause was observed before the needle was removed to prevent cell extravasation. The incision was then sutured and the mice were kept under observation for 1 hour.

For visualize LSEC-Akaluc, each mouse was injected intraperitoneally with 100 μl of Akaluc substrate TokeOni (15 mg/ml; Sigma-Aldrich, no. 808350), and in vivo bioluminescence imaging was initiated after 3 min. 3D in vivo imaging of mice was performed using the In Vivo Imaging System (IVIS) Spectrum device. Image acquisition conditions were as follows: Exposure time was 1 min; field of view was set to D mode for five mice at a time; pixel combination (binning) was set to small; and f/stop was set to 1. Mice were photographed sequentially in four positions: prone, left lateral, supine, and right lateral. Images were analyzed using Living Image 4.3 software (PerkinElmer).

### *Engineering system*

*Hydrogel with adjustable stiffness*. 2D substrates with controlled stiffness were fabricated using PEGDA hydrogel and collagen I. PEGDA precursor solution consisting of 0.2% ammonium persulfate (APS) (w/v); 0.1% *N*,*N*,*N*′,*N*′-tetramethylethylenediamine (TEMED) (w/v); 0.06% (w/v); 1% *N*-succinimidyl acrylate (NSA); 10% *N*-isopropylacrylamide (NIPAM); and 0.5, 2.5, or 15.5% poly(ethylene glycol) diacrylate with a molecular weight of 4000 (PEGDA4000) (w/v) with different concentration in cold PBS (pH 8.0) was dropped onto the 3-(trimethoxysilyl)propyl methacrylate (TMSPMA)–treated coverslip to form hydrogel. All the substrates were coated at 4°C overnight with 0.5% gelatin from porcine skin (Sigma-Aldrich, V900863) dissolved in $diH_2O$, which was proved to be at similar coated concentrations on the substrate surfaces with different stiffness (*6*).

High-concentration collagen (Corning collagen I) was dissolved in 1 M NaOH and DMEM to prepare solution (3 mg/ml) and incubated in 37°C for 1 hour to be gelatinized. 1-Ethyl-3-(3-dimethylaminopropyl) carbodiimide (EDC)/*N*-hydroxysuccinimide (NHS) cross-linking solution (pH 5.4) consisting of 500 mM EDC and 200 mM NHS was further diluted in MES buffer to obtain a mass ratio of EDC:NHS:MES:collagen (1.731:0.415:2.09883:1) for 100% cross-linking of the collagen. Collagen was incubated with 100% cross-linking EDC/NHS solution at room temperature for 12 hours and washed with $Na_2HPO_4$ and $ddH_2O$ for 1 hour on the shaker to achieve higher viscosity. Non–cross-linked and cross-linked collagen were incubated with culture medium at incubator for 1 hour before cell seeding. Quantification of mechanical properties of 2D PEGDA hydrogel and collagen was performed by atomic force microscopy (AFM) and optical tweezers respectively.

*2D static HH chip fabrication*. The 2D static HH chip accommodates 16 hydrogels of varying stiffness that are simultaneously subjected to 4 HPs. It is fabricated from an in-house 3D printed photosensitive resin mold using PDMS with a 10:1 ratio of Sylgard 184 silicone elastomer base and hardener, cured at 40°C for 24 hours. Cells were inoculated in the hydrogel substrate for 12 hours after which the hydrogel was placed into the chamber and sealed with PDMS. Culture medium was perfused into the chamber through a three-way valve for real-time pressure measurement using a digital pressure gauge (Xinsite, HT1890). The ViSiSens oxygen sensing device continuously monitors the oxygen level in the chamber, maintaining conditions similar to those in a cell culture incubator. The chamber allows for HP stimulation in the range of 5 to 20 mmHg, mimicking portal vein pressure in the healthy and late fibrosis human liver, respectively. Control cells were placed in the chamber with no pressure applied.

*3D dynamic HH chip fabrication*. The protocol for the fabrication of engineered blood vessels was modified from previous studies (*52*). For each microfluidic channel, the device consists of two collagen ports with the radius of 4 mm at the spacing of 2 mm and one suspended engineered blood vessel with the diameter of 160 μm formed by needle guide in PDMS. The device was bonded with glass coverslip by plasma cleaner (PDC-32G, Harrick). Each channel was treated with following reagents before lumen fabrication: washed with di-$H_2O$ and 75% ethanol, modified with polylysine at 65°C for 1 hour, modified with 2% glutaraldehyde at room temperature for 45 min, and then washed with 75% ethanol. Lumen was further sterilized under ultraviolet radiation. Collagen (3 mg/ml) was dissolved in DMEM and 1 M NaOH and pipetted into the collagen port. A steel needle (160 μm) pretreated with 5% bovine serum albumin (BSA) at room temperature for 20 min was introduced into the device before polymerization and removed after incubation in 37°C for 5 to create the hollow channel. Collagen was further cross-linked with EDC/NHS solution based on discussed methods. Cell ($5 \times 10^5$/ml) was gently pipette into the channel and turned upside down every 10 min to allow attachment to both sides. Twenty-four hours of perfusion at the flow rate of 1.5 μl/min was performed after 12 hours of static culture to allow formation of single endothelial barrier. Culture medium (DMEM with 10% FBS, 0.5% PS, 0.25% gentamicin, and 1% amphotericin) was added to the top of the collagen port for moisture. For 3D dynamic lumen, same amount of optimized resistance module was connected and placed before or after the lumen to obtain constant wall shear stress and different pressure gradient within the lumen. Lumen was perfused at the flow rate of 1.5 μl/min for 4 hours to achieve normal pressure (≤5 mmHg) or high-pressure gradient (20 mmHg). Pressure was monitored and measured through three-way valve within the perfusion system.

*Permeability test*. Position the vessel such that the whole vessel diameter is within the field of view, and there is gel visible on both sides of the vessel. Add 70-kDa fluorescent dextran solution to the lumen at the flow rate of 1.5 μl/min and acquire image every 30 s for 10 min using time-lapse confocal. Quantification of fluorescence was performed by ImageJ algorithm and permeability was calculated based on following formula

$$P = \frac{1}{I_0 - I_b} \frac{d}{4} \frac{I_2 - I_1}{t_2 - t_1}$$

where $P$ is diffusive permeability, $I_0$ is the initial fluorescence density at $t = 0$, $I_b$ is the background fluorescence density, $I_2$ and $I_1$ is the fluorescence density at $t = t_2$ and $t = t_1$ after and before plateau of fluorescence density increase, respectively.

*Cell stretching*. Cells were seeded in a PDMS chamber, which was precoated with collagen I (BD354236), and equipped with a STREX mechanical strain instrument (B-Bridge International). After 12 hours of culture, allowing the cells to attach to the chamber floor, the chamber was subjected to mechanical strains of 0, 5, 10, or 20%, with 10 cycles per minute for 24 hours. Subsequently, the cells were fixed using 4% paraformaldehyde (PFA) and stained with 4′,6-diamidino-2-phenylindole (DAPI) and F-actin. Cell roundness is calculated by ImageJ.

*Wall shear stress stimulation*. Cells were seeded in parallel plate flow chamber on coverslip coated at 4°C overnight with 0.5% gelatin (Sigma-Aldrich) dissolved in di$H_2O$. The perfusion with wall shear stress at 0, 5, or 10 dyne/cm$^2$ mimicking late fibrosis and healthy sinusoid was achieved through peristaltic pump (Langer), respectively. The cells were then fixed in 4% PFA and stained for DAPI as well as F-actin. Intensity of fluorescence for each channel can be visualized in pseudocolor heatmap.

### Cell-based experiments

*Apoptosis detection*. Apoptosis was detected using annexin V in the Annexin V-FITC kit (C1062L, Beyotime), and propidium iodide (PI) was used to detect necrotic cells or cells with loss of cell membrane integrity in the late stages of apoptosis. For in situ staining characterization, cells that were still affixed to the hydrogel after pressure treatment were washed once with PBS and mixed into buffer with annexin V–fluorescein isothiocyanate (FITC), PI, and Hoechst at ratios of 1:150, 1:300, and 1:1000, respectively, and incubated for 25 min at room temperature away from light. Photographic detection was performed by confocal microscopy (A1RMPSi, Nikon). For flow cytometry assay, cells were digested off the PEGDA hydrogel with trypsin after pressurization treatment, while cells shed free in culture after pressurization were collected and centrifuged at 179*g* for 5 min, and then the cell precipitate was washed once with PBS. Annexin V and PI were added to the buffer at the ratios of 1:200 and 1:400, respectively, and incubated for 30 min on ice and protected from light before resuspension with 200 μl of buffer was resuspended and detected by BD LSRFortessa SORP flow cytometer (BD Biosciences). Flow data were analyzed with FlowJo software.

*cAMP accumulation assay*. To detect intracellular cAMP levels by GPR116 and different mutants of GPR116 in response to HP stimulation or stachel peptide, assays were performed using the Alpha Screen cAMP Assay Kit (PerkinElmer) as follows. LSECs ($1 \times 10^5$) were seeded on a 10-mm-diameter 11-kPa PEG hydrogel and incubated for 12 hours. To prevent cAMP degradation, the medium was replaced with fresh medium containing 500 μM 3-isobutyl-1-methylxanthine and incubated for 30 min. Each cell was treated with 5 μM forskolin for 15 min as a positive control or incubated with 300 μM GPR116 stachel peptide for 15 min or stimulated with 20-mmHg HP for 1 hour. Cells on each hydrogel were gently washed once with PBS and then lysed with 100 μl of lysis buffer (e.g., 5 mM Hepes containing 0.1% BSA and 0.3% Tween 20, pH 7.4) to collect cAMP. Accumulated cAMP was measured in 96-well white OptiPlates (PerkinElmer) using a Fusion-Alpha Multilabel Reader (PerkinElmer) by detecting the absorbance at 560 nm with an EnSight Multimode Microplate Reader (PerkinElmer).

*Mini-Gs protein recruitment assay*. To test whether GPR116 responds to HP through the G-stimulatory protein (Gs) pathway. In a six-well plate, 2 μg of pCAGGS-hGPR116-FL-Igbit-miniGs plasmid was added to HEK293T cells at 70% fusion, and transfection was assisted by the addition of 4 μl of linear polyethyleneimine (2 mg/ml) and 100 μl of Opti-MEM. After 24 hours of transfection, the substrate furimazine (final dilution, 1:1000) was added and incubated for 1 hour. Cells were blown up into single-cell suspensions. A portion of the cells was added to a 96-well plate with $1 \times 10^5$ cells per well, forskolin and stachel peptide were added, and the luminescence traces were recorded for 35 min. Another fraction of cells was added to a 1-ml syringe and processed at 20-mmHg HP for 5 min and then added to a 96-well plate, and the luminescence traces are detected for 30 min.

*RNA sequencing*. Total RNA from the cells was extracted with TRIzol, and 2 μg of each sample was taken for library construction and sequencing. Clean reads from both the mouse pLSECs and human LSECs sample were mapped to the mouse and human genome sequence Ensembl GRCm38 and Ensembl GRCh38, respectively. Differential expression analysis was performed using the DESeq2 program package. Genes were considered to be differentially expressed when the counts data of the gene was greater than 10, there was more than twofold difference in expression and the *q* value was less than 0.01. Functional enrichment analysis of Gene Ontology (GO) and KEGG was performed using the GOstats program package.

To analyze the similarity between the transcriptome features of LSECs in a 2D vascular model in vitro and those in different liver fibrosis stages in vivo, RNA was isolated from pLSECs of normal healthy mice and designated as NC. Additionally, RNA was isolated from pLSECs cultured on a 1.5-kPa substrate and stimulated with low HP of 10 mmHg for 4 hours, designated as Soft + LP, and from pLSECs cultured on 11-kPa substrate and stimulated with high HP of 20 mmHg for 4 hours, designated as Stiff + HP. The RNA of pLSECs from mice with early fibrosis induced by $CCl_4$ for 4 weeks and mice with late fibrosis induced for 12 weeks were 4W and 12W, respectively. Library construction and Illumina sequencing were completed at Biomarker Technology (Beijing, China), and the raw reads for NC, 4W, 12W, Soft + LP, and Stiff + HP were 21.5, 20.7, 19.51, 20.5, and 18.7 million. The DEGs in the 4W, 12W, Soft + LP, and Stiff + HP relative to those in the NC were analyzed separately. DEGs were identified with count of >10, *q* value of <0.01, and $\log_2$ fold change ($\log_2$FC) of > 1 or <−1. Then, the similarity of the DEGs in the in vitro model Soft + LP/NC versus the in vivo early fibrotic endothelium 4 W/NC and the similarity of the DEGs in the in vitro model Stiff + HP/NC versus the in vivo late fibrosis endothelium 12W/NC were analyzed separately. The differential genes of Stiff + HP and Stiff + NP were also analyzed to elucidate the effect of HP on pLSECs.

For screening cell membrane surface proteins on LSECs in response to HP stimulation, DEGs were analyzed in human LSECs cell lines with or without HP. RNA from LSECs cultured on 11-kPa substrate for 12 hours without HP stimulation was NC, and RNA from LSECs stimulated by 4 and 24 hours of 20-mmHg HP was 4h HP and 24h HP, respectively. Library construction and Illumina sequencing were completed at Annoroad Gene Technology (Beijing, China), and the raw reads of the NC, 4h HP, and 24h HP groups were 45.6 million, 44.9 million, and 44.8 million, respectively. The DEGs of 4h HP and 24h HP relative to those of NC were analyzed separately. Then, the overlapping genes of up-expressed genes in 4h HP/NC with down-expressed genes in 24h HP/NC and down-expressed genes in 4h HP/NC with up-expressed genes in 24h HP/NC were compared respectively. Candidate genes were screened among the overlapping genes for relevant expressed proteins located in the plasma membrane and cell surface. The rules for analyzing DEGs here were counts of >10 and *P* values of <0.05. Candidate genes were further screened for specific expression in ECs in the human cirrhotic tissue single-cell sequencing database GSE13503.

For analyzing the effect of GPR116 on LSECs response to HP and the intracellular related signaling pathways. RNA extracted from cells exposed to HP for 4 hours was labeled as shCtrl HP and sh*GPR116* HP, while cells not treated with pressure were labeled as shCtrl NP and sh*GPR116* NP, respectively. Library construction and Illumina sequencing were completed at Annoroad Gene Technology (Beijing, China), and the raw reads for the shCtrl NP, shCtrl HP, sh*GPR116* NP, and sh*GPR116* HP groups were 45.6 million, 46.4 million, 41.8 million, and 41.0 million, respectively. The overlapping genes in the DEGs of sh*GPR116* NP versus shCtrl NP and those of sh*GPR116* HP versus shCtrl HP were analyzed. DEGs were recognized with counts of >10, *q* value of <0.01, and $|\log_2 FC|$ of >1. These overlapping genes were eliminated from the set of DEGs in sh*GPR116* versus shCtrl, and the remaining genes were analyzed by KEGG and GO.

For analyzing the effect of *Gpr116* on hepatic sinusoidal ECs in late fibrosis mice, RNA was extracted from pLSECs of *Cdh5*Cre-ERTx *Gpr116*fl/fl (KO, *n* = 3) and WTx*Gpr116*fl/fl (WT, *n* = 3) mice, respectively. Subsequent to library preparation and Illumina sequencing conducted at GENEWIZ (Soochow, China), DEGs were analyzed using GO and KEGG pathways. DEGs were recognized with counts of >10, *q* value of <0.01, and $|\log_2 FC|$ of >1.

### *Miscellaneous*

*Quantitative reverse transcriptase PCR*. RNA was extracted from the cells, mouse liver tissue, and collagen-cell mixture by lysis with TRIzol (Vazyme, R401-01). Chloroform of 1/5 volume was added to the lysate, mixed thoroughly, and allowed to stand before centrifugation at 12,000*g* at 4°C for 10 min. The upper aqueous phase was collected, and an equal volume of isopropanol was added; after centrifugation at 12000*g* for 10 min, the precipitate was washed with 75% ethanol, dried, and solubilized in deoxyribonuclease/ribonuclease-free water (Solarbio, R1600). After checking the RNA concentration and purity by NANODROP 2000 measurement, cDNA was obtained after reverse transcription using reverse transcriptase (HiScript II Reverse Transcriptase; Vazyme, no. R222). Real-time qPCR experiments were performed in a CFX96 Real-Time PCR Detection System (Bio-Rad). The assay was performed using 2X AceQ qPCR SYBR Green Master Mix (Vazyme). Glyceraldehyde-3-phosphate dehydrogenase or *Gapdh* was used as a reference gene, and relative expression levels were calculated using the 2-ΔΔCT method. The primers are listed in table S3.

*RNA interference and transfection*. Small interfering RNA (siRNA) that targeted the mouse Gpr116 gene was synthesized by XiangHong Co. Ltd. (Beijing, China). The synthesized siRNA sequences were the following: siGpr116 #1, UGGCCAAGGAGGAGAGAAATT; siGpr116 #2, GGACAAAGCUUUUCUAUAATT; and siGpr116 #3, AAGAAUACAUGGUGGAUAUTT. Transfection of synthesized siRNAs was carried out using Lipofectamine RNAiMAX Reagent Agent (Invitrogen) according to the manufacturer's instructions.

*Scanning electron microscopy*. Cell culture on hydrogels was fixed with 2.5% glutaraldehyde for 4 hours at room temperature. Ethanol dehydration of the samples was performed by constant washing with increasing concentration of ethanol from 50 to 100%. Last, the samples were coated with a thin layer of gold and imaged in an ultramicroscope (HITACHI, SU8600).

*Western blot*. HP-treated cells or mouse pLSECs were collected and lysed by blowing and mixing on ice with RIPA (Beyotime) supplemented with protease inhibitors. Samples were deeply fragmented by ultrasound, and protein concentrations were determined using a

BCA protein assay kit (Beyotime, P0010S). Polyacrylamide gel electrophoresis (PAGE; 10%) separator and concentrate gels were prepared using the PAGE Gel Ultra Rapid Preparation Kit (Melun Bio, MA0382). In protein transfer buffer (Melun Bio, MA0094), proteins were transferred to polyvinylidene difluoride membranes (Millipore) with the assistance of a protein transfer buffer (Millipore, MA0094). The membranes were closed for 1 hour at room temperature with 5% skim milk powder prepared in Tris Buffered Saline with Tween-20 (TBST). Primary antibodies were incubated in primary antibody dilution buffer (A1810, Solar) in an overnight shaker at 4°C. TBST was washed three times for 10 min each. The primary antibody was incubated in primary antibody dilution buffer (A1810, Solar) at 4°C overnight on a shaker and washed three times with TBST for 10 min each. Color development was performed with a color development solution, and exposure photos were taken with a LAS4000 biomolecular imager.

*Young's modulus measurement by AFM*. The hydrogel or cells to be measured were fixed on a 25-mm-diameter round slide, which was reproduced onto the AFM adapter and screwed tightly, and the medium was added to ensure that there was no leakage. Young's modulus measurements were performed using a CellHesion 200 system (JPK Instruments). Silicon microspheres with a diameter of 6 μm were adhered to the tip of the AFM cantilever (ARROW-TL1-50, NANOWORLD) with a nominal spring constant of 0.03 N $m^{-1}$. The calibration of cantilever was performed using thermal oscillation method. For measurement of hydrogel stiffness, PEGDA hydrogels were prepared as described previously using 25-mm round slides, or type I collagen hydrogels were fixed to 25-mm round slides using treated 3M adhesive with rough scratches. For measurement of cells, this was done in cell culture medium at a constant temperature of 37°C, attached to the hydrogel as single cells, with AFM cantilever tip microspheres touching the cells avoiding the nucleus and cell edges. The data obtained were analyzed with JPKSPM Data Processing software to calculate the Young's modulus by Hertz model obtained to hydrogel or cell.

*Immunostaining and Sirius Red staining*. For immunofluorescence staining, cells were washed with PBS and fixed with 4% PFA for 30 min. Mouse liver tissues were embedded in optimal cutting temperature compound (OCT) and cut into 6- to 8-μm sections at −20°C. These sections were then pasted onto cationic slides and fixed with 4% PFA for 20 min. After fixation, cells and tissues were washed three times with PBS for 3 min each, and permeabilization was done by incubating with 0.1% Triton X-100 on ice for 10 min. Samples were blocked with 3% BSA for 1 hour at room temperature. Primary antibodies were diluted with 3% BSA and incubated overnight at 4°C. The cells were then washed three times with PBS for 5 min each, followed by incubation with secondary antibodies diluted with 1% BSA. Additionally, Hoechst (Beyotime, catalog no. 33342) was added at a ratio of 1:1000 and incubated for 40 min at room temperature, protected from light. Last, the cells were washed three times with PBS and stored in PBS at 4°C, while the tissue sections were blocked with 5% glycerol and stored away from light. High-quality images were captured using a confocal laser microscope (Nikon A1R HD25).

For immunohistochemical staining, paraffin sections were dewaxed at 65°C for 1.5 hours, followed by dehydration with an ethanol gradient and repair with antigen repair solution (Wuhan ServiceBio). Endogenous peroxidase was blocked by incubating the sections in 3% hydrogen peroxide solution for 25 min at room temperature, protected from light. Then, 3% BSA was used for blocking for 30 min at room temperature, and the sections were incubated overnight at 4°C with GPR116 antibody diluted in PBS at a ratio of 1:100. Subsequently, the sections were incubated with horseradish peroxidase–goat–anti-rabbit secondary antibody for 50 min at room temperature. 3,3′-Diaminobenzidine (DAB) color development was followed by hematoxylin restaining for 3 min. The sections underwent dehydration and clearing with a series of ethanol, *n*-butanol, and xylene treatments. Histological images were taken using a microscope (3DHISTECH Pannoramic SCAN).

For Sirius Red staining, the Modified Sirius Red Stain Kit (no picric acid) (Solarbio, G1472) was used according to the manufacturer's instructions. Whole-tissue slides were scanned on a 3DHISTECH Pannoramic SCAN at ×20 magnification. Sirius Red staining was quantified using ImageJ.

*Measuring the hydroxyproline concentration*. Liver tissues were weighed, digested with 6 M HCl at 110°C for 6 hours until no large tissue clumps were visible, cooled, and the pH adjusted to 7 with 10 M NaOH. The lysed tissue was centrifuged at 16,000 rpm for 20 min at 25°C, and the supernatant was collected. The supernatant was processed with the Hydroxyproline (HYP) Content Assay Kit (Solarbio, BC0255) according to the experimental instructions, and the absorbance value at 560 nm was detected by EnSight Multimode Microplate Reader (PerkinElmer). The HYP content in liver tissue was then quantified.

*Computational fluid dynamics*. Design and modeling of resistance module was performed by SOLIDWORKS (Dassault Systemes, 2020). Fluid dynamics parameters within the microfluidic channel were simulated by Ansys Fluent (Ansys, 2021) with a flow rate of equal to 1.5 μl/min at inlet mimicking physiological conditions within liver sinusoids. Geometry of resistance module was modified accordingly to obtain pressure gradient at 3D lumen lower than 5 mmHg and greater than 20 mmHg to recapitulate portal vein pressure in healthy and cirrhotic liver.

*Analysis of public scRNA-seq data*. Single-cell RNA sequencing (scRNA-seq) data for healthy and cirrhotic liver were analyzed on the basis of previously published database (*53*). DEGs ($q < 0.05$ and absolute value of $\log_2$FC greater than 3) in cirrhotic human LSECs compared to healthy human were screened on the basis of cellular component description on UniProt database (www.uniprot.org/) to identify membrane protein-related genes.

*Quantification and statistical analysis*. Statistical analysis was performed by GraphPad Prism. Significant differences between groups were checked using one-way analysis of variance (ANOVA) following Tukey's multiple comparisons test or unpaired, two-tailed Student's *t* test. One-way ANOVA was used when comparing three or more groups of data, and Student's *t* test was used when determining two groups of data, as indicated in the figure legend. Unless indicated otherwise, all quantification data are presented as means ± SEM. Experiments have at least three independent replicates.

## Supplementary Materials

**This PDF file includes:**
Figs. S1 to S7
Tables S1 to S4
Uncropped blots

## REFERENCES AND NOTES

1. A. M. Moon, A. G. Singal, E. B. Tapper, Contemporary epidemiology of chronic liver disease and cirrhosis. *Clin. Gastroenterol. Hepatol.* **18**, 2650–2666 (2020).

2. J. Gracia-Sancho, G. Marrone, A. Fernandez-Iglesias, Hepatic microcirculation and mechanisms of portal hypertension. *Nat. Rev. Gastroenterol. Hepatol.* **16**, 221–234 (2019).
3. P. Caraceni, J. G. Abraldes, P. Gines, P. N. Newsome, S. K. Sarin, The search for disease-modifying agents in decompensated cirrhosis: From drug repurposing to drug discovery. *J. Hepatol.* **75**, S118–S134 (2021).
4. D. Thabut, V. Shah, Intrahepatic angiogenesis and sinusoidal remodeling in chronic liver disease: New targets for the treatment of portal hypertension? *J. Hepatol.* **53**, 976–980 (2010).
5. M. Zadorozhna, S. Di Gioia, M. Conese, D. Mangieri, Neovascularization is a key feature of liver fibrosis progression: Anti-angiogenesis as an innovative way of liver fibrosis treatment. *Mol. Biol. Rep.* **47**, 2279–2288 (2020).
6. L. Liu, Z. You, H. Yu, L. Zhou, H. Zhao, X. Yan, D. Li, B. Wang, L. Zhu, Y. Xu, T. Xia, Y. Shi, C. Huang, W. Hou, Y. Du, Mechanotransduction-modulated fibrotic microniches reveal the contribution of angiogenesis in liver fibrosis. *Nat. Mater.* **16**, 1252–1261 (2017).
7. J. Ehling, M. Bartneck, X. Wei, F. Gremse, V. Fech, D. Mockel, C. Baeck, K. Hittatiya, D. Eulberg, T. Luedde, F. Kiessling, C. Trautwein, T. Lammers, F. Tacke, CCL2-dependent infiltrating macrophages promote angiogenesis in progressive liver fibrosis. *Gut* **63**, 1960–1971 (2014).
8. S. Lefere, F. Van de Velde, A. Hoorens, S. Raevens, S. Van Campenhout, A. Vandierendonck, S. Neyt, B. Vandeghinste, C. Vanhove, C. Debbaut, X. Verhelst, J. Van Dorpe, C. Van Steenkiste, C. Casteleyn, B. Lapauw, H. Van Vlierberghe, A. Geerts, L. Devisscher, Angiopoietin-2 promotes pathological angiogenesis and is a therapeutic target in murine nonalcoholic fatty liver disease. *Hepatology* **69**, 1087–1104 (2019).
9. C. Audebert, G. Peeters, P. Segers, W. Laleman, D. Monbaliu, H. Korf, J. Trebicka, I. E. Vignon-Clementel, C. Debbaut, Closed-loop lumped parameter modeling of hemodynamics during cirrhogenesis in rats. *IEEE Trans Biomed. Eng.* **65**, 2311–2322 (2018).
10. Y. Long, Y. Niu, K. Liang, Y. Du, Mechanical communication in fibrosis progression. *Trends Cell Biol.* **32**, 70–90 (2022).
11. J. H. Park, S. B. Jo, J.-H. Lee, H.-H. Lee, J. C. Knowles, H.-W. Kim, Materials and extracellular matrix rigidity highlighted in tissue damages and diseases: Implication for biomaterials design and therapeutic targets. *Bioact. Mater.* **20**, 381–403 (2023).
12. M. Ortega-Ribera, A. Gibert-Ramos, L. Abad-Jordà, M. Magaz, L. Téllez, L. Paule, E. Castillo, R. Pastó, B. de Souza Basso, P. Olivas, L. Orts, J. J. Lozano, R. Villa, J. Bosch, A. Albillos, J. C. García-Pagán, J. Gracia-Sancho, Increased sinusoidal pressure impairs liver endothelial mechanosensing, uncovering novel biomarkers of portal hypertension. *JHEP Rep.* **5**, 100722 (2023).
13. E. E. Friedrich, Z. Hong, S. Xiong, M. Zhong, A. Di, J. Rehman, Y. A. Komarova, A. B. Malik, Endothelial cell Piezo1 mediates pressure-induced lung vascular hyperpermeability via disruption of adherens junctions. *Proc. Natl. Acad. Sci. U.S.A.* **116**, 12980–12985 (2019).
14. J. Xu, J. Mathur, E. Vessières, S. Hammack, K. Nonomura, J. Favre, L. Grimaud, M. Petrus, A. Francisco, J. Li, V. Lee, F. L. Xiang, J. K. Mainquist, S. M. Cahalan, A. P. Orth, J. R. Walker, S. Ma, V. Lukacs, L. Bordone, M. Bandell, B. Laffitte, Y. Xu, S. Chien, D. Henrion, A. Patapoutian, GPR68 senses flow and is essential for vascular physiology. *Cell* **173**, 762–775.e16 (2018).
15. I. Rozenberg, S. H. Sluka, L. Rohrer, J. Hofmann, B. Becher, A. Akhmedov, J. Soliz, P. Mocharla, J. Borén, P. Johansen, J. Steffel, T. Watanabe, T. F. Lüscher, F. C. Tanner, Histamine H1 receptor promotes atherosclerotic lesion formation by increasing vascular permeability for low-density lipoproteins. *Arterioscler. Thromb. Vasc. Biol.* **30**, 923–930 (2010).
16. Y. Zou, H. Akazawa, Y. Qin, M. Sano, H. Takano, T. Minamino, N. Makita, K. Iwanaga, W. Zhu, S. Kudoh, H. Toko, K. Tamura, M. Kihara, T. Nagai, A. Fukamizu, S. Umemura, T. Iiri, T. Fujita, I. Komuro, Mechanical stress activates angiotensin II type 1 receptor without the involvement of angiotensin II. *Nat. Cell Biol.* **6**, 499–506 (2004).
17. H.-B. Kwon, S. Wang, C. S. M. Helker, S. J. Rasouli, H.-M. Maischein, S. Offermanns, W. Herzog, D. Y. R. Stainier, In vivo modulation of endothelial polarization by Apelin receptor signalling. *Nat. Commun.* **7**, 11805 (2016).
18. S. Mueller, Does pressure cause liver cirrhosis? The sinusoidal pressure hypothesis. *World J. Gastroenterol.* **22**, 10482–10501 (2016).
19. E. Felli, S. Selicean, S. Guixé-Muntet, C. Wang, J. Bosch, A. Berzigotti, J. Gracia-Sancho, Mechanobiology of portal hypertension. *JHEP Rep.* **5**, 100869 (2023).
20. S. S. Desai, J. C. Tung, V. X. Zhou, J. P. Grenert, Y. Malato, M. Rezvani, R. Espanol-Suner, H. Willenbring, V. M. Weaver, T. T. Chang, Physiological ranges of matrix rigidity modulate primary mouse hepatocyte function in part through hepatocyte nuclear factor 4 alpha. *Hepatology* **64**, 261–275 (2016).
21. S. Mueller, L. Sandrin, Liver stiffness: A novel parameter for the diagnosis of liver disease. *Hepat. Med.* **2**, 49–67 (2010).
22. W. C. Yeh, P. C. Li, Y. M. Jeng, H. C. Hsu, P. L. Kuo, M. L. Li, P. M. Yang, P. H. Lee, Elastic modulus measurements of human liver and correlation with pathology. *Ultrasound Med. Biol.* **28**, 467–474 (2002).
23. K. T. Suk, D. J. Kim, Staging of liver fibrosis or cirrhosis: The role of hepatic venous pressure gradient measurement. *World J. Hepatol.* **7**, 607–615 (2015).
24. M. Yin, K. J. Glaser, A. Manduca, T. Mounajjed, H. Malhi, D. A. Simonetto, R. Wang, L. Yang, S. A. Mao, J. M. Glorioso, F. M. Elgilani, C. J. Ward, P. C. Harris, S. L. Nyberg, V. H. Shah, R. L. Ehman, Distinguishing between hepatic inflammation and fibrosis with MR elastography. *Radiology* **284**, 694–705 (2017).
25. R. Reiter, M. Shahryari, H. Tzschätzsch, M. Haas, C. Bayerl, B. Siegmund, B. Hamm, P. Asbach, J. Braun, I. Sack, Influence of fibrosis progression on the viscous properties of in vivo liver tissue elucidated by shear wave dispersion in multifrequency MR elastography. *J. Mech. Behav. Biomed. Mater.* **121**, 104645 (2021).
26. Y. Zhu, X. Chen, X. Zhang, S. Chen, Y. Shen, L. Song, Modeling the mechanical properties of liver fibrosis in rats. *J. Biomech.* **49**, 1461–1467 (2016).
27. G. Peeters, C. Debbaut, P. Cornillie, T. De Schryver, D. Monbaliu, W. Laleman, P. Segers, A multilevel modeling framework to study hepatic perfusion characteristics in case of liver cirrhosis. *J. Biomech. Eng.* **137**, 051007 (2015).
28. S. Lemoinne, A. Cadoret, P.-E. Rautou, H. E. Mourabit, V. Ratziu, C. Corpechot, C. Rey, N. Bosselut, V. Barbu, D. Wendum, G. Feldmann, C. Boulanger, C. Henegar, C. Housset, D. Thabut, Portal myofibroblasts promote vascular remodeling underlying cirrhosis formation through the release of microparticles. *Hepatology* **61**, 1041–1055 (2015).
29. N. Li, X. Zhang, J. Zhou, W. Li, X. Shu, Y. Wu, M. Long, Multiscale biomechanics and mechanotransduction from liver fibrosis to cancer. *Adv. Drug Deliv. Rev.* **188**, 114448 (2022).
30. C. Niaudet, J. J. Hofmann, M. A. Mäe, B. Jung, K. Gaengel, M. Vanlandewijck, E. Ekvärn, M. D. Salvado, A. Mehlem, S. Al Sayegh, L. He, T. Lebouvier, M. Castro-Freire, K. Katayama, K. Hultenby, C. Moessinger, P. Tannenberg, S. Cunha, K. Pietras, B. Laviña, J. Hong, T. Berg, C. Betsholtz, Gpr116 receptor regulates distinctive functions in pneumocytes and vascular endothelium. *PLOS ONE* **10**, e0137949 (2015).
31. C. Niaudet, M. Petkova, B. Jung, S. Lu, B. Laviña, S. Offermanns, C. Brakebusch, C. Betsholtz, Adgrf5 contributes to patterning of the endothelial deep layer in retina. *Angiogenesis* **22**, 491–505 (2019).
32. H. H. Lin, K. F. Ng, T. C. Chen, W. Y. Tseng, Ligands and beyond: Mechanosensitive adhesion GPCRs. *Pharmaceuticals* **15**, 219 (2022).
33. C. A. Dessalles, C. Leclech, A. Castagnino, A. I. Barakat, Integration of substrate- and flow-derived stresses in endothelial cell mechanobiology. *Commun. Biol.* **4**, 764 (2021).
34. J. Li, B. Hou, S. Tumova, K. Muraki, A. Bruns, M. J. Ludlow, A. Sedo, A. J. Hyman, L. McKeown, R. S. Young, N. Y. Yuldasheva, Y. Majeed, L. A. Wilson, B. Rode, M. A. Bailey, H. R. Kim, Z. Fu, D. A. L. Carter, J. Bilton, H. Imrie, P. Ajuh, T. N. Dear, R. M. Cubbon, M. T. Kearney, K. R. Prasad, P. C. Evans, J. F. X. Ainscough, D. J. Beech, Piezo1 integration of vascular architecture with physiological force. *Nature* **515**, 279–282 (2014).
35. S. S. Ranade, S.-H. Woo, A. E. Dubin, R. A. Moshourab, C. Wetzel, M. Petrus, J. Mathur, V. Bégay, B. Coste, J. Mainquist, A. J. Wilson, A. G. Francisco, K. Reddy, Z. Qiu, J. N. Wood, G. R. Lewin, A. Patapoutian, Piezo2 is the major transducer of mechanical forces for touch sensation in mice. *Nature* **516**, 121–125 (2014).
36. K. Shibasaki, TRPV4 activation by thermal and mechanical stimuli in disease progression. *Lab. Invest.* **100**, 218–223 (2020).
37. K. Brown, A. Filuta, M. G. Ludwig, K. Seuwen, J. Jaros, S. Vidal, K. Arora, A. P. Naren, K. Kandasamy, K. Parthasarathi, S. Offermanns, R. J. Mason, W. E. Miller, J. A. Whitsett, J. P. Bridges, Epithelial Gpr116 regulates pulmonary alveolar homeostasis via Gq/11 signaling. *JCI Insight* **2**, (2017).
38. S. Prömel, H. Waller-Evans, J. Dixon, D. Zahn, W. H. Colledge, J. Doran, M. B. Carlton, J. Grosse, T. Schöneberg, A. P. Russ, T. Langenhan, Characterization and functional study of a cluster of four highly conserved orphan adhesion-GPCR in mouse. *Dev. Dyn.* **241**, 1591–1602 (2012).
39. K. R. Monk, J. Hamann, T. Langenhan, S. Nijmeijer, T. Schöneberg, I. Liebscher, Adhesion G protein-coupled receptors: From in vitro pharmacology to in vivo mechanisms. *Mol. Pharmacol.* **88**, 617–623 (2015).
40. T. F. Franke, C. P. Hornik, L. Segev, G. A. Shostak, C. Sugimoto, PI3K/Akt and apoptosis: Size matters. *Oncogene* **22**, 8983–8998 (2003).
41. J. Peltier, A. O'Neill, D. V. Schaffer, PI3K/Akt and CREB regulate adult neural hippocampal progenitor proliferation and differentiation. *Dev. Neurobiol.* **67**, 1348–1361 (2007).
42. C. Li, J. Tian, G. Li, W. Jiang, Y. Xing, J. Hou, H. Zhu, H. Xu, G. Zhang, Z. Liu, Z. Ye, Asperosaponin VI protects cardiac myocytes from hypoxia-induced apoptosis via activation of the PI3K/Akt and CREB pathways. *Eur. J. Pharmacol.* **649**, 100–107 (2010).
43. S. Guixe-Muntet, M. Ortega-Ribera, C. Wang, S. Selicean, I. Andreu, J. Z. Kechagia, C. Fondevila, P. Roca-Cusachs, J. F. Dufour, J. Bosch, A. Berzigotti, J. Gracia-Sancho, Nuclear deformation mediates liver cell mechanosensing in cirrhosis. *JHEP Rep.* **2**, 100145 (2020).
44. M. Ortega-Ribera, A. Fernandez-Iglesias, X. Illa, A. Moya, V. Molina, R. Maeso-Diaz, C. Fondevila, C. Peralta, J. Bosch, R. Villa, J. Gracia-Sancho, Resemblance of the human liver sinusoid in a fluidic device with biomedical and pharmaceutical applications. *Biotechnol. Bioeng.* **115**, 2585–2594 (2018).
45. Y. Du, G. Khandekar, J. Llewellyn, W. Polacheck, C. S. Chen, R. G. Wells, A bile duct-on-a-chip with organ-level functions. *Hepatology* **71**, 1350–1363 (2020).
46. S. Ya, W. Ding, S. Li, K. Du, Y. Zhang, C. Li, J. Liu, F. Li, P. Li, T. Luo, L. He, A. Xu, D. Gao, B. Qiu, On-chip construction of liver lobules with self-assembled perfusable hepatic sinusoid networks. *ACS Appl. Mater. Interfaces* **13**, 32640–32652 (2021).

47. K. J. Jang, M. A. Otieno, J. Ronxhi, H. K. Lim, L. Ewart, K. R. Kodella, D. B. Petropolis, G. Kulkarni, J. E. Rubins, D. Conegliano, J. Nawroth, D. Simic, W. Lam, M. Singer, E. Barale, B. Singh, M. Sonee, A. J. Streeter, C. Manthey, B. Jones, A. Srivastava, L. C. Andersson, D. Williams, H. Park, R. Barrile, J. Sliz, A. Herland, S. Haney, K. Karalis, D. E. Ingber, G. A. Hamilton, Reproducing human and cross-species drug toxicities using a Liver-Chip. *Sci. Transl. Med.* **11**, (2019).
48. A. Gough, A. Soto-Gutierrez, L. Vernetti, M. R. Ebrahimkhani, A. M. Stern, D. L. Taylor, Human biomimetic liver microphysiology systems in drug development and precision medicine. *Nat. Rev. Gastroenterol. Hepatol.* **18**, 252–268 (2021).
49. G. G. Ernstrom, M. Chalfie, Genetics of sensory mechanotransduction. *Annu. Rev. Genet.* **36**, 411–453 (2002).
50. A. Rabiee, G. Garcia-Tsao, E. B. Tapper, Nonselective Beta-blockers in portal hypertension: Why, when, and how? *Clin. Liver Dis.* **19**, 118–123 (2022).
51. F. T. Bu, P. C. Jia, Y. Zhu, Y. R. Yang, H. W. Meng, Y. H. Bi, C. Huang, J. Li, Emerging therapeutic potential of adeno-associated virus-mediated gene therapy in liver fibrosis. *Mol. Ther. Methods Clin. Dev.* **26**, 191–206 (2022).
52. W. J. Polacheck, M. L. Kutys, J. B. Tefft, C. S. Chen, Microfabricated blood vessels for modeling the vascular transport barrier. *Nat. Protoc.* **14**, 1425–1454 (2019).
53. P. Ramachandran, R. Dobie, J. R. Wilson-Kanamori, E. F. Dora, B. E. P. Henderson, N. T. Luu, J. R. Portman, K. P. Matchett, M. Brice, J. A. Marwick, R. S. Taylor, M. Efremova, R. Vento-Tormo, N. O. Carragher, T. J. Kendall, J. A. Fallowfield, E. M. Harrison, D. J. Mole, S. J. Wigmore, P. N. Newsome, C. J. Weston, J. P. Iredale, F. Tacke, J. W. Pollard, C. P. Ponting, J. C. Marioni, S. A. Teichmann, N. C. Henderson, Resolving the fibrotic niche of human liver cirrhosis at single-cell level. *Nature* **575**, 512–518 (2019).

**Acknowledgments:** We would like to acknowledge the Laboratory Animal Resources Center (Tsinghua University, Beijing, China) for technical support; H. Cao and J. Wang at NIKON Biological Imaging Center (Tsinghua University, Beijing, China) and J. Wang and Y. Sun at Cell Biology Facility (Tsinghua University, Beijing, China) for assistance with confocal microscopy imaging techniques; Y. Zhang at Imaging Core Facility (Tsinghua University, Beijing, China) for intravital imaging of mouse liver; and Y. Liu at Cell Function Analysis Facility, Technology Center for Protein Sciences (Tsinghua University, Beijing, China), for assistance with technical of flow cytometry. Schematic was created with BioRender.com. **Funding:** This work was supported by the National Natural Science Foundation of China (nos. 32430058, 82125018, and 32401086), the Beijing Natural Science Foundation (no. Z230016), and the Chinese Postdoctoral Science Foundation (no. 2022 M721862). **Author contributions:** Conceptualization: Y.D. and Y.L. Data curation: Y.L., R.L., Y.J., Z.W., Y.D., and Z.L. Formal analysis: Y.L., K.L., Y.N., R.W., R.L., Y.J., Z.W., and Z.L. Investigation: Y.L., K.L., Y.N., R.W., Y.Z., Y.A., B.W., Y.J., Z.W., and Z.L. Methodology: Y.L., K.L., Y.N., Y.Z., Y.A., Y.D., and B.W. Project administration: Y.D. and Y.L. Resources: Y.D., Y.L., R.L., X.Z., X.L., and B.L. Validation: Y.L., K.L., Y.N., and R.W. Visualization: Y.L., K.L., R.W., Y.N., Y.D., and R.L. Writing—original draft: Y.L. and Y.D. Writing—review and editing: Y.L., Y.D., K.L., R.L., and X.Q. Funding acquisition: Y.D. and Y.L. Supervision: Y.D. **Competing interests:** The authors (Y.D. and Y.L.) disclose that a patent application (China patent application no. CN118759198A, filed on 11 October 2024) related to the findings in this manuscript is now pending. The authors declare that they have no competing interests. **Data and materials availability:** All data needed to evaluate the conclusions in the paper are present in the paper and/or the Supplementary Materials. The high-throughput sequencing data are publicly available at the National Centre for Biotechnology Information with Gene Expression Omnibus with accession number GSE244784.

Submitted 24 November 2024
Accepted 14 October 2025
Published 14 November 2025
10.1126/sciadv.adu7596